AD-752 628

HELICOPTER ROTOR WAKE GEOMETRY AND AIR-LOADS AND DEVELOPMENT OF LASER DOPPLER VELOCIMETER FOR USE IN HELICOPTER ROTOR WAKES

M. P. Scully, et al

Massachusetts Institute of Technology

Prepared for:

Naval Air Systems Command

August 1972

MASSACHUSETTS INSTITUTE OF TECHNOLOGY
AEROPHYSICS LABORATORY

Technical Report 179

Helicopter Rotor Wake Geometry and Airloads and

Development of Laser Doppler Velocimeter for Use

in Helicopter Rotor Wakes

by

M. P. Scully and J. P. Sullivan

August 1972

D D C

RECEIVED

DEC 11 1972

B

APPROVED FOR PUBLIC RELEASE;
DISTRIBUTION UNLIMITED

Distribution of this report is unlimited.

DOCUMENT CONTROL DATA - R & D

(Security classification of title, body of abstract and indexing annotation must be entered when the overall report is classified)

1 ORIGINATING ACTIVITY (Corporate author)	2a. REPORT SECURITY CLASSIFICATION
Massachusetts Institute of Technology Department of Aeronautics and Astronautics Cambridge, Massachusetts 02139	UNCLASSIFIED
	2b. GROUP

3 REPORT TITLE

HELICOPTER ROTOR WAKE GEOMETRY AND AIRLOADS AND DEVELOPMENT OF LASER DOPPLER VELOCIMETER FOR USE IN HELICOPTER ROTOR WAKES

4. DESCRIPTIVE NOTES *(Type of report and inclusive dates)*

Final Scientific Report covering the period June 6, 1971 to June 6, 1972

5. AUTHOR(S) *(First name, middle initial, last name)*

M. P. Scully
J. P. Sullivan

6. REPORT DATE	7a. TOTAL NO. OF PAGES	7b. NO. OF REFS
August 1972	59	11

8a. CONTRACT OR GRANT NO	9a. ORIGINATOR'S REPORT NUMBER(S)
Contract No. N00019-71-C-0220	TR 179
b. PROJECT NO.	
c.	9b. OTHER REPORT NO(S) *(Any other numbers that may be assigned this report)*
d.	

10. DISTRIBUTION STATEMENT

Distribution of this report is unlimited.

11 SUPPLEMENTARY NOTES	12. SPONSORING MILITARY ACTIVITY
	U. S. Naval Air Systems Command Department of the Navy Washington, D. C. 20360

13. ABSTRACT

Computer programs have been developed for the calculation of helicopter rotor tip vortex geometry in hover and forward flight and for the calculation of helicopter rotor harmonic airloads in forward flight. Calculated forward flight tip vortex geometries compare well in general with experimental smoke studies although there are differences in detail. The hovering tip vortex geometry agrees qualitatively with experiment but does not move downward fast enough. Airloads were computed using both the classical rigid wake assumption and the distorted tip vortex geometry obtained from the computer program. When compared with experimental airloads measurements the rigid wake airloads give better results than the distorted wake airloads. This is due to excessive peak heights in the distorted wake airloads. The problem is thought to be the neglect of some unknown but important effects which limit peak heights due to close blade vortex interactions.

A two dimensional laser Doppler velocimeter (LDV) has been developed for use in helicopter rotor wakes. Extensive measurements were made in vortex rings. From this data the circulation, streamlines and vorticity distribution were calculated. Finally, the construction of a hollow composite material rotor for use with the laser system is discussed.

Details of illustrations in
this document may be better
studied on microfiche

14. KEY WORDS	LINK A		LINK B		LINK C	
	ROLE	WT	ROLE	WT	ROLE	WT
HELICOPTER WAKE						
HELICOPTER AIR LOADS						
LASER DOPPLER VELOCIMETER						
VORTEX RINGS						

1b

Massachusetts Institute of Technology
Department of Aeronautics and Astronautics
Aerophysics Laboratory

Technical Report 179

Helicopter Rotor Wake Geometry and Airloads and

Development of Laser Doppler Velocimeter for Use

in Helicopter Rotor Wakes

by

M. P. Scully and J. P. Sullivan

August 1972

Distribution of this report is unlimited.

1C

FOREWORD

This work at Massachusetts Institute of
Technology was sponsored by the Naval Air
Systems Command under contract No.
N00019-71-C-0220. The contract was monitored
by Mr. Ray Malatino.

ABSTRACT

Computer programs have been developed for the calcula-
tion of helicopter rotor tip vortex geometry in hover and
forward flight and for the calculation of helicopter rotor
harmonic airloads in forward flight. Calculated forward
flight tip vortex geometries compare well in general with
experimental smoke studies although there are differences
in detail. The hovering tip vortex geometry agrees quali-
tatively with experiment but does not move downward fast
enough. Airloads were computed using both the classical
rigid wake assumption and the distorted tip vortex geometry
obtained from the computer program. When compared with
experimental airloads measurements the rigid wake airloads
give better results than the distorted wake airloads. This is
due to excessive peak heights in the distorted wake airloads.
The problem is thought to be the neglect of some unknown but
important effects which limit peak heights due to close blade
vortex interactions.

A two dimensional laser Doppler velocimeter (LDV) has
been developed for use in helicopter rotor wakes. Extensive
measurements were made in vortex rings. From this data the
circulation, streamlines and vorticity distribution were cal-
culated. Finally, the construction of a hollow composite
material rotor for use with the laser system is discussed.

iii

TABLE OF CONTENTS

Section I

Section II

FIGURE CAPTIONS

Fig. 1.   a.   Reference Beam System
             b.   Dual Scatter System

Fig. 2.   Doppler shift vs. velocity for He-Ne laser at
             various scattering angles

Fig. 3.   a.   Reference Beam System
             b.   Dual Scatter System

Fig. 4.   a.   Doppler signal from .0002 dia. wire passing
                  through center of probe volume.

             b.   Doppler signal from .0002 dia. wire which did
                  not pass through center of probe volume.

             c.   Doppler signal from spinning disk.

Fig. 5.   Signals from Reference Beam and Dual Scatter
             Systems

Fig. 6.   One-dimensional LDV system

Fig. 7.   Beam pattern for two-dimensional LDV looking
             toward laser

Fig. 8.   Two-dimensional LDV system

Fig. 9.   Time diagrams for electronic system

Fig. 10.   Demodulation of Test Signal

Fig. 11.   Linearity and velocity check using spinning disc

Fig. 12.   Vortex ring

Fig. 13.   Velocity distribution through vortex ring

Fig. 14.   Coordinate system for vortex ring data analysis

v

NOMENCLATURE

a   vortex ring radius

$\hat{a}_{1,2}$ unit vectors defined in Fig. 1

$\hat{b}_{1,2}$ unit vectors defined in Fig. 1

c   velocity of light

d   diameter of particle

$\hat{e}_{s_1}$ unit vector in direction of polarization of E_s

$\hat{e}_{s_2}$ unit vector in direction of E_s

$\vec{E}_R$ electric field of reference beam

$\vec{E}_s$ electric field of scattered radiation

$\vec{E}_{s_1}$ electric field of scattered radiation from Beam No. 1

$\vec{E}_{s_2}$ electric field of scattered radiation from Beam No. 2

f   frequency

f_o frequency of laser

f_D Doppler shift

I_{RB} intensity of scattered radiation from reference beam system

I_{DS} intensity of scattered radiation from dual scatter system

$\hat{k}_I$ unit vector in direction of incident laser beam

$\hat{k}_s$ unit vector in direction of scattered radiation

$\hat{k}_{1,2}$ unit vector in direction of beam No. 1 or No. 2

r_o radius of vortex ring

r,Z   polar coordinates

t	time
U	velocity in Z direction
U_O	velocity of vortex ring
V	velocity in r direction
$\vec{V}$	velocity of particle
Γ	circulation
Γ_O	total circulation
θ	scattering angle
λ	wavelength of laser
ψ	stream function
ω	vorticity

HELICOPTER ROTOR WAKE GEOMETRY AND AIRLOADS WORK

This section summarizes research done on the computation of helicopter rotor wake geometry in both hovering and forward flight and the effects of wake geometry on rotor harmonic airloads in forward flight. This work is part of a continuing program of research in this area, and a more detailed discussion of the results of this work plus research done in previous years will be published in Reference 1.

FORWARD FLIGHT WAKE GEOMETRY

The only concentrated vortex line in the rotor wake is the tip vortex. The primary source of high harmonic airloads and hence vibration is close interactions between this concentrated tip vortex and the rotor blades. In order to predict the airloads due to these close interactions the geometry of the tip vortex must be known accurately. The classical rigid wake geometry assumption based on uniform inflow is not accurate enough for this purpose. It is necessary to include the distortion of the tip vortex geometry by the actual non-uniform and time-varying induced velocities experienced by the tip vortex. These induced velocities are a function, primarily, of the tip vortex geometry which is in turn a function of the induced velocities. Thus the computation of the tip vortex distortion and hence the geometry require the integration of the Biot-Savart relation for induced velocities over the wake which must be repeated (or updated) as the knowledge of the actual geometry of the wake improves. This is a very time-consuming process requiring the use of a large and expensive computer program.

Digital computer programs have been developed at M.I.T. and elsewhere to compute the tip vortex distortion. These programs are generally more than an order of magnitude more expensive than the corresponding airloads computation for a given wake geometry. This is prohibitively expensive for use in routine airloads computations. Research effort has therefore been concentrated on reducing the expense of wake geometry computations as well as improving their accuracy.

Most of the expense of a wake geometry computation comes from the repeated integrations of the Biot-Savart relation for induced velocities over the wake. Thus the best way to save computation is to maximize the efficiency of the Biot-Savart relation integrations and to minimize the number of them. The most efficient way to integrate the Biot-Savart relation over a distorted vortex line is to break the line up into a series of short straight line segments. The integration can be performed in closed form for a straight line segment. Thus the integral

1

for the entire line is obtained by adding up the contributions
of all of the straight line segments. The length of the
straight line segments is a trade-off between accuracy and
expense. A highly distorted tip vortex may require segments
subtending 15° or less in azimuth for adequate representation.

To minimize the number of straight vortex line segments
whose contribution to the induced velocity must be computed
the simplest possible wake model is used. The wake is divided
up into the trailing wake due to radial circulation variations
and the shed wake due to azimuthal circulation variations.
The outboard portion of the trailing wake rolls up to form a
concentrated tip vortex which is the dominant feature of the
wake and must be accurately represented. The tip vortex is
modeled by a series of straight vortex line segments forming
a single vortex line. These vortex line segments have a
finite radius viscous core. The initial core radius is esti-
mated at about 10% of the blade chord based on experimental
data. After a segment of the tip vortex undergoes a close
interaction with a rotor blade it is assumed to have burst,
increasing the core radius to about four times the original
radius.

The shed wake and the inboard portion of the trailing
wake remain spread out in vortex sheets near the rotor. Due
to their spread-out nature the exact location of these por-
tions of the wake is not important and the rigid wake geo-
metry assumption can be used. It is important, however, to
avoid introducing unrealistic induced velocity peaks due to
the use of powerful concentrated vortex lines to represent
these portions of the wake. A common method is to use a
large number of vortex lines to represent the inboard trailing
wake. This is very expensive so a better way is needed.

For the most accurate representation of the inboard trail-
ing and shed wakes, vortex sheets should be used. The Biot-
Savart relation can be integrated over a rectangular, planar
vortex sheet segment in closed form. The inboard trailing and
shed wakes can therefore be represented by a series of such
vortex sheet segments. The first attempts to use vortex sheets
involved representing the inboard trailing wake with one set
of vortex sheet segments and the shed wake with two sets, one
having constant radial circulation and the other linear radial
circulation. This adds up to three vortex sheet segments and
one vortex line segment (for the tip vortex), per azimuth com-
pared to three vortex line segments per azimuth for the all
vortex line model. Since the computation of the induced velo-
city contribution of a vortex sheet segment is more than twice

as expensive as the same computation for a vortex line segment this model proved to be nearly three times as expensive as the vortex line model. The results of tip vortex geometry computations using this vortex sheet model gave better agreement with experimental results than computations using the vortex line model however. Since the circulation of the shed wake is normally almost an order of magnitude less than the trailing wake a model was tried using a single large core vortex line with linear radial circulation for the shed wake, plus one set of vortex sheets for the inboard trailing wake and a vortex line for the tip vortex. This gives the same results as the original vortex sheet model and costs only 40 percent more than the vortex line model and has been adopted as standard.

After choosing a wake model the number of updatings of the integration of the Biot-Savart relation must be minimized to save computation. A big saving can be made by dividing the wake elements contributing to the induced velocity at a point P into near and far wake elements relative to point P. The induced velocity contribution of each wake element varies roughly inversely with the square of the distance from each element to point P. Therefore the induced velocity contributions of far wake elements at point P do not need to be updated nearly as often as the contributions of the near wake elements.

The M.I.T. wake geometry program is iterative starting with the rigid wake assumption. An iteration ends when the distortion of $2\pi m$ (typically $m = 2$) in azimuth of newly generated wake has been computed. The next iteration starts assuming the distortion computed by the previous iteration. The induced velocity contributions of each far wake element at each point P are computed only once per iteration. The induced velocity contributions of the near wake elements are updated several times during an iteration but not at every azimuth (time) interval.

An iteration in the wake geometry computation proceeds by advancing the rotor in discrete azimuth steps thus generating new wake. The induced velocity and hence the tip vortex distortion is computed only at the boundary between the new wake generated during the current iteration and the old wake from the previous iteration. As more wake is generated its contribution to the induced velocity is added in while the contributions of the rest of the wake are assumed to remain constant. After n azimuth steps the induced velocity contributions from the entire wake are recomputed (updated) to account for the movement of the boundary point under the influence of the previously computed induced velocities and to account for the improved knowledge of the wake geometry. This updating is done

independently for the boundary point at each different azimuth. The updating parameter n is a function of azimuth and smaller values are used at the sides of the rotor where the tip vortices of the various blades and successive turns of each tip vortex cross, resulting in large tip vortex distortions. In addition the tip vortex distortion of all of the wake generated so far in the current iteration is updated every ℓ azimuth steps. This involves recomputing the induced velocity and hence the distortion at all of the points in the new wake, not just at the boundary between the old and the new wake. This is much more expensive than simply updating the induced velocity at the boundary and hence is not done as frequently. Since the entire new wake is involved, this type of updating is done at all azimuths, so ℓ is not a function of azimuth.

To speed up convergence of the wake geometry it is important to use the best available knowledge of the wake geometry at all points in the computation. Thus, if the contribution of a wake element in the old wake is being computed, the distortion at that wake element is determined by taking the distortion accumulated at that azimuth up to its arrival at the boundary between the old and new wakes, as computed for the new wake, and adding in the old wake distortion for the time after it left the boundary. This same principle is applied in the middle of an update when the first part of the new wake has been updated but the last part has not. Since the old wake does not extend to infinity, and in fact is just as long as the new wake at the end of an iteration, extrapolation is used to find the geometry of wake elements beyond the end of the old wake. This ensures that there is always a realistic representation of the wake beyond the boundary between the old and new wakes, even when this boundary reaches the lower end of the old wake.

During wake geometry computations using this program the location of some wake elements tends to oscillate. These oscillations may take six or more iterations to converge to a final solution, which is very expensive. To damp these oscillations more rapidly the first step is to average the distortions obtained from successive iterations. This is still too slow, so the averaging of the distortions obtained from successive updates is used. This normally results in convergence within two iterations.

The wake is not the only source of induced velocity and hence distortion. The bound vorticity also makes a significant contribution. The bound vorticity is represented by a single vortex line at the quarter chord line of the blade. The distortion is computed at points every 15 degrees or so along the tip vortex. In cases where the tip vortex passes

4

close under or over the blade and roughly perpendicular to it
the contribution of the bound vorticity to the distortion is
largely determined by the distance from the blade-tip vortex
crossing to the nearest point on the tip vortex at which the
distortion is computed. Since these points are about 15 degrees
or a quarter of the rotor radius apart, this results in large,
random variations in the contribution of the bound vorticity to
the distortion. The way to avoid this problem is to actually
integrate over time the induced velocity at a point P on the
tip vortex as the blade passes under or over it, instead of
computing the induced velocity at two different times 15 degrees
in azimuth apart and multiplying the average by delta time. It
turns out that representing the bound vorticity by a vortex
sheet segment 15 degrees wide is the same as performing this
integral directly. Therefore the vortex sheet representation
of the bound vorticity is used whenever the tip vortex passes
close over or under a blade. This should not be confused with
a lifting surface representation of the bound vorticity. It is
only a method of integrating the effect of a lifting line over
time.

The wake geometry program has been tested for 1, 2 and 4
bladed cases. The results show better agreement with experi-
ment than the old wake geometry program developed under the
previous contract. In addition faster convergence and faster
execution have been achieved. The developments which produced
these improvements are: the modified vortex sheet wake model,
the inclusion of vortex core bursting, the vortex sheet repre-
sentation of the bound vorticity, improved updating procedures
including making n a function of azimuth, improved procedures
for always using the most recent wake geometry information,
and averaging the distortion from successive updates.

The wake geometry program has been run for various values
of the computational parameters n, ℓ, and d_m (a parameter which
determines the split between the near and far wakes). Values
of these parameters have been found which give a good cost-
accuracy trade-off. In addition the effects of vortex core
size and various wake models have been evaluated. These
results will be presented in more detail in Reference 1.

EFFECTS OF WAKE GEOMETRY ON HARMONIC AIRLOADS

The primary reason for computing the tip vortex distortion
is to improve the accuracy of harmonic airloads computations.
Therefore airloads computations have been made using both rigid
and distorted wake models for 2, 4 and 6 bladed rotors for which
experimental airloads data are available. Unfortunately there
is no case for which both experimental airloads and tip vortex
geometry are available. However, comparison with experimental
tip vortex geometry data for cases where no experimental airloads

data are available has shown that the results of the wake
geometry program are generally in agreement although there are
local differences.

The wake geometry program is normally run in conjunction
with the airloads program. The first step is to make a rigid
wake airloads run. The circulation distribution and the loca-
tion of any vortex core bursting is input from this run into
the wake geometry program. The tip vortex geometry obtained
from this run is then used in a second airloads run. This
process continues as long as necessary. Normally one wake
geometry run and two airloads runs are sufficient, but some-
times the circulation distribution and/or the distribution
of vortex core bursting may change radically due to tip
vortex distortion. In this case a second wake geometry run
and a third airloads run will be needed.

The airloads program uses a wake model similar to the
large core vortex line model of the wake geometry program
including vortex core bursting. Under the next contract
the airloads program will be modified to use a single vortex
sheet plus two vortex lines wake model similar to the latest
wake geometry program. A vortex sheet segment is used for the
shed wake element immediately behind the blade and the inte-
gration over the shed wake is carried to within ε of the
control points on the blade, where ε is determined from
lifting surface theory.

Whenever the tip vortex passes close under or over a
blade a rapid radial variation in lift and hence circulation
is produced on the blade. This in turn results an extra trail-
ing wake being generated. This extra trailing wake could be
represented by a many (~20) trailing vortex line near wake model
but this is expensive and neglects lifting surface effects
which become important for very close blade-tip vortex inter-
actions. Instead the approximations developed in Reference 2
using lifting surface theory are used whenever the tip vortex
passes close over or under a blade. In addition the vortex
core is assumed to burst (increase by about a factor of 4 in
size) after a close blade-tip vortex interaction.

Once the induced velocity field has been determined the
airloads and circulation distribution are computed. Rigid body
flapping and first mode flapwise bending are included but lag
and torsion are neglected. Provision is made for flapping
hinge offset and a spring at the flapping hinge. Reverse
flow, radial flow, and dynamic stall effects are included.
Iteration is used to obtain a converged circulation distribu-
tion. To save computation a matrix of influence coefficients
is computed for a given wake geometry, which, when multiplied
by the circulation matrix, gives the induced velocity matrix.
Most of the computation in an airloads run is in finding the
influence coefficient matrix. The circulation iteration
using that matrix is very fast.

6

The case most carefully studied so far is a four bladed
rotor at an advance ratio of 0.18. For this case the rigid
wake airloads computation gives good overall results when
compared with experimental data. The distorted wake airloads
computation improves agreement in some local areas but overall
is much worse than the rigid wake. The basic problem is
larger peaks in the theoretical airloads than in the experimental
ones. The distorted wake is worse than the rigid wake because
the wake is closer to the rotor, especially over the forward
edge of the rotor. The tip vortex geometry is probably generally
correct, with possible local exceptions, because the tip vortex
should be closer to the rotor than rigid wake would predict
over the forward edge of the rotor, since this is an area of
upwash from the tip vortices of the preceding blades. There-
fore the problem is inadequate treatment of close blade-tip
vortex interactions, despite all of the special provisions
made for this so far.

The better results obtained by the rigid wake model are
due to compensating errors, the reduction in peak size caused
by the wake being too far away from the blades being compen-
sated by neglect of close blade-tip vortex interaction effects
which if included would have reduced peak sizes. The most
likely close blade-tip vortex effects are: local separation
or stall on the blade due to the intense induced velocities
resulting in steep local pressure gradients, vortex burst-
ing over or under the blade instead of behind it, the possibility
that some of the tip vortex circulation is not wrapped up into
a tight vortex core but is spread out in spiral vortex sheets
around the core, and local tip vortex distortion near the blade.
The first two effects are being studied in a flow visualiza-
tion program at M.I.T. The third effect is suggested by the
fact that some investigators find only 60% or so of the bound
circulation in the tip vortex core, for example, Reference 3.

The wake geometry program is only intended to provide the
gross tip vortex geometry. It only computes the tip vortex
distortion at points 15 degrees or so apart and a lifting line
is used to represent the blade. To compute the local tip vor-
tex distortion near a blade the rest of the wake can be neglected
but the blade must be more carefully represented. At least a
lifting surface representation will be needed and thickness
effects may turn out to be important as well.

In summary, the rigid wake model gives good results due to
compensating errors. To improve on the rigid wake results
it will be necessary to use distorted tip vortex geometry in
conjunction with a much more careful treatment of close blade-
tip vortex interaction effects.

7

HOVERING WAKE GEOMETRY

A specialized version of the wake geometry program has been developed for the hovering case. This program uses the assumption of azimuthal symmetry to save computation. Since there is no inflow due to forward speed, and since the wake is not swept downstream by the forward speed, more of the wake is important than for a forward flight wake geometry computation. Therefore an infinite vortex cylinder is added to the wake model starting at the lower end of the normal wake model and continuing to infinity. Due to the assumption of azimuthal symmetry there is no shed wake. In addition to the standard options of a rigid wake inboard trailing vortex line or vortex sheet, as in forward flight, there is provision for a tilted inboard trailing vortex sheet with its outer edge moving down faster than its inner edge. This last option is based on experimental data on the inboard trailing sheet geometry from Reference 4. Other than the above mentioned modifications the hovering wake geometry program is similar to the forward flight wake geometry program described previously.

Great difficulty was experienced in obtaining converged solutions from the hovering wake geometry program. Averaging of the distortion from successive updates, as described previously for the forward flight program, was originally developed for the hovering case. Using this averaging, plus very careful treatment of the wake beyond the lower bound of wake geometry computation, including the infinite vortex cylinder, fairly good convergence is obtained after 6 to 8 iterations. The resulting wake geometry does not move down as fast or contract as fast as the experimental results of Reference 4 indicate it should.

In addition some recent unpublished theory by Professor Widnall at M.I.T. indicates that an infinite helical vortex cylinder is always unstable. Since, after the first turn or so, the hovering tip vortex is a semi-infinite helical vortex cylinder, it is also likely to be unstable. This explains the difficulty in obtaining a converged solution. The converged solutions that were finally obtained are based on the use of averaging of the distortion between successive updates. This averaging is in turn based on the assumption that a converged solution exists. The net result is to introduce some extra damping into the system which does not exist in the real world. In addition the wake geometry is only computed every 20 degrees in azimuth which means that short wave length instabilities do not show up. The converged tip vortex geometry produced by this program probably represents some sort of average location of the tip vortex and may be useful as such.

8

The tip vortex near the rotor is the part of the wake which is important for airloads or performance computations. This part of the wake appears to be stable in the real world as shown in the experimental results of Reference 4. Therefore effort should be concentrated on computing the geometry of this part of the tip vortex. The results of the current hovering wake geometry program do not go down fast enough or contract fast enough in this area, when compared to experiment. Hand computations show that this problem is very sensitive to small changes in the geometry, since the net induced velocity on an element of the tip vortex is normally the small difference of large numbers. This suggests that even a very small amount of wind or recirculation could have significant effects on the tip vortex geometry.

In summary, the current hovering wake geometry program developed from the forward flight wake geometry program does not give satisfactory results. A completely new hovering wake geometry program should be developed, independent of the forward flight program, which concentrates on computing the geometry of the first part of the tip vortex. This new program should be designed to separate out the effects of the various contributors to tip vortex distortion (i.e. the bound vorticity, the curvature of the tip vortex, the tip vortices of the other blades, the returning part of the tip vortex itself, the inboard trailing wake, etc.). Using this tool, a better understanding of the relative importance of the various parts of the problem can be obtained and used to develop a solution.

9

REFERENCES

1. Scully, M. P., "Computation of Helicopter Rotor Wake Geometry and Its Influence on Rotor Harmonic Airloads," M.I.T. Dept of Aeronautics and Astronautics, PhD Thesis (to be published).

2. Johnson, W. R., "A Lifting Surface Solution for Vortex Induced Airloads and Its Application to Rotary Wing Airloads Calculations," M.I.T. Aeroelastic and Structures Research Laboratory, Technical Report TR 153-2, April 1970.

3. Chigier, N. A. and Corsiglia, V. R., "Tip Vortices - Velocity Distributions," 27th Annual National V/STOL Forum of the American Helicopter Society, Preprint S22, May 1971.

4. Landgrebe, Anton T., "An Analytical and Experimental Investigation of Helicopter Rotor Hover Performance and Wake Geometry Characteristics," USAAAMRDL Tech. Report 71-24, June 1971.

SECTION II

DEVELOPMENT OF LASER DOPPLER VELOCIMETER
FOR USE IN HELICOPTER ROTOR WAKES

INTRODUCTION

Traditionally the velocity of a time varying flow field
has been measured using a hot-wire anemometer. The use of a
hot wire in the wake of a helicopter (or any flow containing
concentrated vorticity) poses two serious problems: probe
interference (possibly in the form of vortex breakdown) and
calibration in a flow field whose direction and magnitude is
rapidly varying. For these reasons a laser Doppler veloci-
meter (LDV) has been developed.

First the basic principles involved in an LDV system are
discussed and then a two-dimensional LDV system is described.
This system is used for extensive measurements on vortex rings.
Finally the construction of a hollow composite material rotor
for use with the LDV system is discussed.

BASIC PRINCIPLES OF LASER DOPPLER VELOCIMETRY

Since the introduction of the laser Doppler velocimeter
(LDV) in 1965 by Yeh and Cummings (Ref 1) numerous systems
have been reported. Two of these, the cross beam -- reference
beam system (Fig. 1a) of ref 2, and the dual scatter system
(Fig. 1b) of refs 3 and 4 will be analyzed. These two were
chosen because they are self aligning; that is, once the beams
are made to intersect at the probing point and pass throug.
the aperature in front of the photomultiplier tube, the system
is aligned. This eliminates the tedious alignment and vibration
problems of other systems.

Laser light that is scattered from particles (smoke, dirt,
polystyrene spheres) moving at th· local fluid velocity* under-
goes a Doppler shift given by

$$f = f_o + \frac{\vec{V} \cdot (\hat{R}_3 - \hat{R}_1)}{\lambda} + O\left(\frac{|\vec{V}|}{c}\right) \tag{1}$$

----

*The difference between the fluid and particle velocities is
estimated in the Appendix.

where

f_o, λ, $\hat{k}_I$ = frequency, wavelength and unit vector in the propagation direction of the incident laser beam

$\vec{V}$ = velocity of particle

$\hat{k}_s$ = unit vector in the direction that the scattered light is detected

c = velocity of light

The frequency of the scattered radiation f, which is of the order of light frequencies ($\sim$5 x 10^{14} cy/sec) can be detected either directly using a Fabry-Perot interferometer or can be heterodyned with some light wave at a known frequency to obtain a signal whose frequency is equal to the shift of the laser light frequency. The present resolution of Fabry-Perot interferometers is only $\sim$2MHz which implies a velocity resolution of $\sim$10 ft/sec. For the present study this is inadequate so a heterodyning system is used.

In the two types of heterodyne systems studied the cross-beam reference beam system (Fig. 1a) heterodynes the scattered radiation with radiation at the laser frequency f_o and the dual scatter system (Fig. 1b) heterodynes the scattered radiation of two different incident beams. In both cases the difference frequency is calculated, using Eq. 1 and the geometry of Fig. 1, to be

$$f_D = \frac{2\ U\ \sin\ \theta/2}{\lambda}$$

where U is the velocity component in a direction perpendicular to the bisector of the angle between two beams. Fig. 2 shows f_D versus U for various values of θ with λ = 6328Å, the wavelength of a He Ne laser. It should be noted that there is a 180° ambiguity in determining direction of U. The plus or minus direction of U must be determined by prior knowledge or flow visualization.

The output signal of the photomultiplier (P.M.) tube is proportioned to the intensity which for the reference beam system is

$$I_{RB} = \left(\vec{E}_R + \vec{E}_s\right) \cdot \left(\vec{E}_R + \vec{E}_s\right)^*$$

$$I_{RB} = \left|\vec{E}_R\right|^2 + \left|E_s(t)\right|^2 + \vec{E}_R \cdot \vec{E}_s(t) \cos\left(2\pi f_D t\right)$$

12

when a single particle traverses the measuring volume. This produces an output like that shown in Fig. 3a. The d.c. level is essentially constant since $E_s(t) << E_c$. The a.c. component is modulated by the term, $E_R E_s(t)$ which is generally a gaussian.

In the dual scatter system the light scattered from one beam is heterodyned with light scattered from the other beam resulting in

$$I_{DS} = \left| \vec{E}_{s_1}(t) \right|^2 + \left| \vec{E}_{s_2}(t) \right|^2 + \vec{E}_{s_1}(t) \cdot \hat{E}_{s_2}(t) \cos\left(2\pi f_D t\right)$$

The results for $E_{s_1}(t) = E_{s_2}(t)$ are shown in Fig. 3b. The d.c. component is now replaced by a low frequency component. The actual signal when a .0002 wire traverses the measuring volume is shown in the oscilloscope trace of Fig. 4a. When the wire doesn't pass through the center of the measuring volume a signal (Fig. 4b) containing a large amount of the low frequency component and small amount of the Doppler signal component is obtained.

In the present investigation more than one scatterer will be in the measuring volume at one time resulting in a signal which is the sum of the signals from individual particles. A typical "continuous" signal for a dual scatter system is shown in Fig. 4c. This signal was obtained from a rotating ground glass disk. It shows the general features of a dual scattering; namely, a low frequency component and low frequency modulation of the Doppler signal. The low frequency modulation is a result of random constructive and destructive interference among the waves scattered by many particles, causing the signal to go randomly to zero during severe destructive interference. This phenomenon, called "drop-out", and the low frequency component, are the major problems in the electronic processing of the signal.

A comparison of the frequency spectrums of the two systems is shown in Fig. 5 for scattering from a ground glass disk and a turbulent jet. Although the magnitudes of the signals are about equal, the low frequency components in the dual scatter system is greater.

The object of this investigation is to determine which of the two systems will give a better signal-to-noise ratio. The

13

reference beam system has the advantage that the signal can be increased by increasing the strength of the reference beam. However, the solid angle through which scattered light may be collected is limited since the Doppler shift $\frac{\vec{V} \cdot (\hat{k}_S - \hat{k}_2)}{\lambda}$ is a function of viewing direction $\hat{k}_s$ so that at large solid angles the Doppler frequency would be unacceptably broadened. On the other hand, the frequency $\frac{\vec{V} \cdot (\hat{k}_{I_1} - \hat{k}_{I_2})}{\lambda}$ of a dual scatter system depends only on the incident beam directions $\hat{k}_{I_1}, \hat{k}_{I_2}$ so that the solid angle for viewing scattered radiation is unlimited. However, the strength of the signal from a dual scatter system is determined entirely by the scattering process. Also there will be more low frequency components in the dual scatter system.

In order to complete the calculations the quantities E_s, E_{s_1} and E_{s_2} must be found which requires a detailed study of the actual scattering process. This study is not yet complete but will be reported at a later date.

The effect of polarization on the intensity of the signal is seen by letting the direction of polarization of the incident beams be given by the unit vector e with appropriate subscript. It is assumed and experiments confirm that the polarization is not changed by the scattering process, so for the dual scatter system

$$\vec{E}_{s_1} = E_{s_1}\hat{e}_{s_1} = E_{a_1}\hat{a}_1 + E_{b_1}\hat{b}_1$$

$$\vec{E}_{s_2} = E_{s_2}\hat{e}_{s_2} = E_{a_2}\hat{a}_2 + E_{b_2}\hat{b}_2$$

where the directions $\hat{a}, \hat{b}$ are shown in Section AA of Fig. 1.

The Doppler shift term of the intensity is proportional to

$$\vec{E}_{s_1} \cdot \vec{E}_{s_2} = \left[-E_{a_1}E_{a_2}\cos\Theta + E_{b_1}E_{b_2} \right] \tag{2}$$

For arbitrary polarization, Eq. 1 shows that the signal decreases as θ increases. If the incident beams are linearly polarized in the $\hat{b}_1$ and $\hat{b}_2$ (i.e. $E_{a_1} = E_{a_2} = 0$) directions then the maximum signal will be obtained.

14

At the present time, the investigation does not indicate which system is better. The experiments indicate that both systems perform well.

TWO DIMENSIONAL LDV SYSTEM AND ASSOCIATED ELECTRONICS

The LDV system constructed for extensive measurements is a dual scatter system. A one-dimensional dual scatter system is shown in Fig. 6. The laser beam is divided by a standard prism-type beamsplitter with a non-absorbing beamsplitting interface. This method of dividing the laser beam is preferable to other systems using mirrors and beamsplitters since only one standard optical component is needed and the path lengths (distance from laser to measuring point) of two beams are equal.

A two-dimensional system is constructed by adding a second beamsplitter (rotated 90 degrees with respect to the first) to form four parallel beams. The pattern of the four beams is shown in Fig. 7. The polarization of the beams is chosen to maximize the signal (Eq. 1) and to eliminate crosstalk between the two dimensions. By placing an analyzing polaroid in front of the P.M. tube either of the velocity components can be chosen with no interference from the other component. This is possible because the polarization is changed only slightly by the scattering process. In the present system, both components are processed simultaneously through one P.M. tube using the electronic system described below. A photograph of the two-dimensional LDV system is shown in Fig. 8. The two components could be processed separately by splitting the scattered radiation with a polarizing type beamsplitter and using two P.M. tubes and two sets of electronics.

The electronic system for processing the LDV signal is one suggested by Ref. 5 for use with periodic flow fields. This "sampling" system will be described for use with periodically produced vortex rings in terms of the time diagrams of Fig. 9 and the equipment layout of Fig. 6. The function generator initiates a pulse which is amplified and used to drive a loudspeaker which forms a vortex ring at a sharp edged orifice. A synchronous pulse is also taken off of the function generator (Fig. 9a).

The velocity versus time, as the vortex ring goes past the measuring point, is shown in Fig. 9b. This is proportional to the frequency versus time of the output signal of the P.M. tube which is fed into the input of the spectrum analyzer. This synchronous pulse from the function generator initiates a time delay which starts the sawtooth sweep generator (Fig. 9c) for the spectrum analyzer after a time t_D. The linear sawtooth represents the center frequency of the narrow filter of the spectrum analyzer. When the frequency from the P.M. tube is equal to the instantaneous frequency of the narrow band pass filter of the spectrum analyzer a "pip" will occur on the spectrum analyzer face and at the spectrum analyzer output (Fig. 9d).

15

This condition can be determined by superposing Fig. 9c on Fig. 9b. The linear sawtooth is fed to the input of a gate which is only opened when a "pip" occurs on the spectrum analyzer. The output of the gate -- in this case, three spots -- is stored on a storage oscilloscope. The three spots correspond to a zero frequency marker and two points on the velocity versus time curve we wish to determine. By varying the time delay the remaining points on the velocity curve can be stored.

The results of demodulating a test oscillator signal varying from 50 kHz to 950 kHz at a rate of 33 Hz are shown in Fig. 10.

The entire LDV system was checked by measuring two components of the velocity of a spinning disk as the disk was traversed across the measuring point. The x component of velocity $U = - \omega y$ should be a constant and the y component $V = \omega x$ should vary linearly as the disk moves in the x direction. The results of this check, shown in Fig. 11, indicate that the linearity of the electronics system is excellent and that the velocity error is within the error in determining the r.p.m. of the disk. The ambiguity in determining the direction of U and V is demonstrated in Fig. 11. The U component is always negative and the V component is negative for negative values of X.

The two dimensional system has been used to measure the velocity distribution in periodically produced vortex rings (smoke rings). (The results of extensive measurements are presented in the next section.) The rings are similar to a helicopter rotor wake since regions of time varying concentrated vorticity are produced, yet the flow field is simpler since it is axisymmetric. A picture of a vortex ring is shown in Fig. 12 and the corresponding velocity distributions in Fig. 13. The velocity curves are the U and V components of velocity versus time as the vortex ring travels by the fixed measuring point. There is a 180° ambiguity in the velocity vector (since frequency is always positive). Flow visualization indicates that the U component is always positive while the V component is positive to the left of the central zero and negative to the right.

TWO DIMENSIONAL MEASUREMENTS OF VORTEX RINGS

Once the principle of using an LDV system for measuring velocities in vortex rings was demonstrated, detailed surveys of two vortex rings (denoted Ring No. 1 and Ring No. 2) were made. Complete two dimensional data were taken for Ring No. 1 but only the component of velocity in the direction of ring travel was measured for Ring No. 2.

The data are treated in the following quasi-steady manner. The LDV system measures velocity versus time at a fixed point in space as the vortex ring goes by the measuring point. The velocity distribution is transformed to the steady coordinate system of Fig. 14 by letting $Z = U_o t$ where U_o is the instantaneous velocity of the vortex ring at the measuring point. The

16

quasi-steady approximation assumes that the properties of the
vortex ring do not change (due to entrainment of surrounding
fluid or wake shedding) significantly in the time it takes
the vortex ring to pass the measuring point. This is justi-
fied by flow visualization studies of the variation of ring
speed U_o and size of the ring. The radius of the ring r_o is
defined as the point of zero velocity along $Z = 0$ in the steady
coordinate system of Fig. 14. Also note that all the data to
be presented are on the "bottom half" of vortex ring as shown
in Fig. 14. A summary of the data is given in Table 1.

Two typical data curves for velocities in the vicinity of
the core of Ring No. 1 are shown in Fig.15. An increase in
scatter over the data in Fig. 13 is evident due to time delay,
jitter, slight variations in the ring position, and possibly
velocity fluctuations in the core. Prior to data analysis
the Polaroid oscilloscope pictures are photographically
enlarged 2.5 times and a smooth curve drawn through the numer-
ous dots. The results of this enlargement are shown in Fig. 16
and 17. These curves represent a portion of the data taken on
Ring No. 1. The remaining data on Ring No. 1 were taken in the
vicinity of the core with an expanded velocity scale.

The U component of velocity versus r along $Z/r_o = 0$ for
the two vortex rings is shown in Fig. 18. The corresponding
curve for Hill's spherical vortex is shown for comparison in
this and the following graphs. The value of r_o the ring
radius and the core radius are defined by this curve. The
core radius a is defined as one-half the distance between the
positive and negative peak velocities. This gives a ratio of
core radius to ring radius of $a/r_o = .27$ for Ring No. 1 and

$a/r_o = .075$ for Ring No. 2, indicating that Ring No. 2 is a
relatively thin core ring while Ring No. 1 has a relatively
fat core but not nearly as fat as Hill's vortex where $a/r =$
1.414. No data were taken in the core of Ring No. 2 due to the
lack of smoke particles in the vicinity of the core. This
defect of smoke particles is shown in Fig. 12 which is a ring
very similar to Ring No. 2.

A circulation Γ is obtained by integrating the velocity
along the curve C of Fig. 14. The curve is a rectangle with
one side a line along $r = $ constant and the other sides tend-
ing to infinity. Thus

$$\Gamma = \int_{-\infty}^{\infty} (u(z) - u_o)\, dz$$
$$\text{ON}$$
$$r = \text{CONST.}$$

In order to correct for the finite extent of the data it is
assumed that $(U(z)-U_o) \sim 1/Z^3$ after the last data point, which
gives

17

$$\Gamma = \int_{Z_1}^{Z_2} (u(z) - u_o)dz + \frac{1}{2}\left[u(z_2) z_2 - u(z_1) z_1 \right]$$

where z_2 is the upstream cutoff and z_1 is the downstream cutoff.

The circulation was determined by finding the area under the curves of Fig. 16 using a planimeter and adding a small correction ($\leq 5\%$) due to the finite extent of the data. The total circulation Γ_o is the integral along $r = 0$. The result of these calculations is shown in Fig. 19. The meaning of the curves is similar to that of Fig. 18 indicating Ring No. 2 is the thinnest core ring having the circulation more concentrated near $r/r_o = 1.0$. The circulation calculated in this manner can give some indication of the vorticity distribution by differentiating the curves of Fig. 19. However, in order to obtain the vorticity this derivative would have to be multiplied by an appropriate length corresponding to the distribution of vorticity in the Z direction. That is, the slope of the curves of Fig. 19 represents the vorticity weighted by an axial distribution length which is unknown.

Since complete two-dimensional data were taken on Ring No. 1, further data analysis is possible. The streamlines and vorticity distribution throughout Ring No. 1 are calculated below.

The streamlines are found by plotting lines of constant streamfunction ψ. The streamfunction ψ is calculated by integrating the velocity along appropriate curves. For an axisymmetric flow

$$d\psi = rUdr - rVdz$$

Integrating from $Z = +\infty$ along a line $r = $ constant gives

$$\psi(r = \text{const}, z) - \psi(r = \text{const}, \infty) = -r \int_{-\infty}^{z} V(z')dz'$$

Assuming that $V \sim 1/z^3$ after some cutoff z_1 and non-dimensionalizing

$$\frac{\psi(r,z)}{r_o^2 u_o} + \frac{1}{2}\left(\frac{r}{r_o}\right)^2 = \frac{r}{r_o}\left[\frac{V(z_1)z_1}{2 u_o r_o} - \int_{z_1}^{z} \frac{V(z'/r_o)}{u_o}d\left(\frac{z'}{r_o}\right) \right] \quad (2)$$

The streamfunction is thus determined by integrating the curves of Fig. 17 with the results shown in Fig. 20.

The streamfunction along $Z = 0$ is found by integrating the U component of velocity in Fig. 18.

18

$$\frac{\psi(r,o)}{r_o^2 u_o} = \int_0^{r/r_o} \left(\frac{r'}{r_o}\right) \frac{u(r'/r_o)}{u_o} d\left(\frac{r'}{r_o}\right) \qquad (3)$$

The results of this integration are shown in Fig. 21. Also shown are the values of $\frac{\psi(r,o)}{r_o^2 U_o}$ calculated from Eq. 2. This critical check shows that the overall consistency of the data is excellent.

The actual streamlines are shown superposed on a photograph of Ring No. 1 in Fig. 22.

The vorticity, ω, is calculated along $Z = 0$ by differentiating the data

$$\frac{\omega(r,o)}{(u_o/r_o)} = \frac{\partial \left(\frac{v}{u_o}\right)}{\partial \left(\frac{z}{r_o}\right)}\Bigg|_{z=0} - \frac{\partial \left(\frac{u}{u_o}\right)}{\partial \left(\frac{r}{r_o}\right)}\Bigg|_{z=0}$$

The first term is the slope of the curves of Fig. 17 at $Z = 0$ and the second term is obtained by differentiating the smoothed curve of Fig. 18. The results of differentiating (Fig. 23) show scatter in the vicinity of the core. This is caused in part by the directional ambiguity of the LDV system. The V component of velocity rapidly changes from a large positive value to a large negative value giving data curves (Fig. 15b) in which the determination of the slope at $V = 0$ is difficult.

The vorticity distribution (Fig. 24) shows the expected concentration of vorticity in the core. The vorticity at any point in the flow field is known, since $\omega/r = F(\psi)$, in a steady axisymmetric flow. The function $F(\psi)$ is shown in Fig. 25. Again this shows scatter in the values of ω/r for $r/r_o < 1$ and $r/r_o > 1$; however, the shape of the resulting curve is the same in both cases.

The problem of stability of vortex rings was treated in a separate study and reported in Ref. 6. The conclusion of Ref. 6 is that vortex rings are unstable to azimuthal perturbations. The measurements presented here were all taken prior to instability.

19

CONSTRUCTION OF A ROTOR FOR USE WITH LDV SYSTEM

A two bladed rotor with hollow rotor blades was designed and constructed. The hollow blade permits smoke to be deposited at the tips or any other place along the blade.

A cross section of the blade in Fig. 26 shows the epoxy-fiberglass structure with a stainless steel spar, beryllium-copper inner chamber and a tungsten rod to maintain balance about the quarter chord. Initially an aluminum model was machined from which a mold (Fig. 27a) was cast of Stycast 2850, a high strength casting resin.

The beryllium-copper was spot-welded to the stainless steel spar and the tungsten rod silver soldered on the front of it. An inner mandrel was inserted inside the beryllium-copper and the outside wrapped with fiberglass wet with Eccomold L-28 laminating resin. This structure was compressed in the mold to form the NACA-0012 airfoil section. After the epoxy cured, the blade was removed from the mold and the inner mandrel removed. The resulting hollow blades are shown in Fig. 27b and 27c.

The drive stand for the rotor (Fig. 28) has a hollow shaft to allow smoke to pass to the rotor. The shaft is driven by a 1/2 h.p., 10,000 rpm motor.

At the present time the rotor has been operated at speeds up to 6,000 rpm. Velocity measurements in the wake of this rotor will be presented in the next contracting period.

20

APPENDIX

MOTION OF SPHERICAL PARTICLES IN A FLOW FIELD

AN LDV measures the velocity of particles in a fluid flow.
In the present experiment oil particles were generated by a
Farval vortex mist lubricator, a device normally used for lubri-
cating high speed bearings. The oil particles are generated
by mechanically breaking up oil drops at a sonic orifice. This
results, after filtering, in cold oil particles in the micron
diameter size range. This method of obtaining particles was
found to be extremely convenient.

In order to estimate the difference between fluid and par-
ticle velocities the equation of motion of the particle is non-
dimensionalized and the appropriate dimensionless parameters
derived.

The equation of motion of a small spherical particle sub-
ject to Stokes drag is (Ref. 7)

$$\frac{\pi}{6} d^3 \rho_p \frac{d\vec{U}_p}{dt} = -3\pi \nu_f \rho_f d(\vec{U}_p - \vec{U}_f) - \frac{\pi}{6} d^3 \nabla p$$

$$- \frac{1}{2} \frac{\pi}{6} d^3 \rho_f \left(\frac{d\vec{U}_p}{dt} - \frac{d\vec{U}_f}{dt} \right)$$

where $\vec{U}$ = velocity
ρ = density
ν = viscosity
d = diameter of particle

Subscripts p and f refer to particle and
fluid respectively.

Non-dimensionalizing with respect to a reference fluid velocity
U_{REF} and length L_{REF} and using

$$\Delta p = -\rho_f \frac{d\vec{U}_f}{dt}$$

$$Stk \frac{d}{dt'} (\vec{U}_p' - B \vec{U}_f') + (\vec{U}_p' - \vec{U}_f') = 0 \qquad \text{(A-1)}$$

21

where all quantities are nondimensional and

$$Stk = \text{Stokes number} = \frac{U_{REF}}{L_{REF}} (1 + \frac{\rho_f}{\rho_p}) \tau$$

$$\tau = \frac{d^2}{18 \, \nu_f} \left(\frac{\rho_p}{\rho_f}\right)$$

$$B = 3 \left(\frac{\rho_f}{\rho_p}\right)\left(\frac{1}{2 + \rho_f/\rho_p}\right)$$

In the present study oil particles are used in air, so $\frac{\rho_f}{\rho_p} \simeq 10^{-3}$

implying $B \simeq 0$ and $Stk = \frac{U_{REF}}{L_{REF}} \tau$.

The role of the time scale τ can be seen by considering the simple problem of a particle moving in a straight line with a velocity at $t = 0$ of U_o in a stationary fluid. At any time t later the velocity will be

$$\frac{U_p}{U_o} = e^{-t/\tau}$$

showing that τ is the characteristic time for a particle to reach the local fluid velocity.

For one micron diameter oil particle in air $\tau = 4 \times 10^{-6}$ sec and the Stokes number, which is a measure of the difference between fluid and particle velocities, is

$Stk = 4 \times 10^{-3}$ for $U_{REF} = 10$ ft/sec and $L_{REF} = .01$ ft.

APPENDIX

MOTION OF SPHERICAL PARTICLES IN A FLOW FIELD

AN LDV measures the velocity of particles in a fluid flow. In the present experiment oil particles were generated by a Farval vortex mist lubricator, a device normally used for lubricating high speed bearings. The oil particles are generated by mechanically breaking up oil drops at a sonic orifice. This results, after filtering, in cold oil particles in the micron diameter size range. This method of obtaining particles was found to be extremely convenient.

In order to estimate the difference between fluid and particle velocities the equation of motion of the particle is nondimensionalized and the appropriate dimensionless parameters derived.

The equation of motion of a small spherical particle subject to Stokes drag is (Ref. 7)

$$\frac{\pi}{6} d^3 \rho_p \frac{d\vec{u}_p}{dt} = -3\pi \nu_f \rho_f d(\vec{u}_p - \vec{u}_f) - \frac{\pi}{6} d^3 \nabla p$$

$$- \frac{1}{2} \frac{\pi}{6} d^3 \rho_s \left(\frac{d\vec{u}_p}{dt} - \frac{d\vec{u}_f}{dt} \right)$$

where $\vec{U}$ = velocity
ρ = density
ν = viscosity
d = diameter of particle

Subscripts p and f refer to particle and fluid respectively.

Non-dimensionalizing with respect to a reference fluid velocity U_{REF} and length L_{REF} and using

$$\Delta p = - \rho_f \frac{d\vec{U}_f}{dt}$$

$$Stk \frac{d}{dt'}(\vec{u}_p' - B \vec{u}_f') + (\vec{u}_p' - \vec{u}_f') = 0 \quad \text{(A-1)}$$

21

where all quantities are nondimensional and

$$\text{Stk} = \text{Stokes number} = \frac{U_{REF}}{L_{REF}} (1 + \frac{\rho_f}{\rho_p}) \tau$$

$$\tau = \frac{d^2}{18\,\nu_f} \left(\frac{\rho_p}{\rho_f}\right)$$

$$B = 3\left(\frac{\rho_f}{\rho_p}\right)\left(\frac{1}{2 + \rho_f/\rho_p}\right)$$

In the present study oil particles are used in air, so $\frac{\rho_f}{\rho_p} \doteq 10^{-3}$

implying $B \doteq 0$ and $\text{Stk} = \frac{U_{REF}}{L_{REF}} \tau$.

    The role of the time scale τ can be seen by considering the simple problem of a particle moving in a straight line with a velocity at $t = 0$ of U_o in a stationary fluid. At any time t later the velocity will be

$$\frac{U_P}{U_o} = e^{-t/\tau}$$

showing that τ is the characteristic time for a particle to reach the local fluid velocity.

    For one micron diameter oil particle in air $\tau = 4 \times 10^{-6}$ sec and the Stokes number, which is a measure of the difference between fluid and particle velocities, is

$\text{Stk} = 4 \times 10^{-3}$ for $U_{REF} = 10$ ft/sec and $L_{REF} = .01$ ft.

Table 1

DATA SUMMARY

	R(ft)	V_o ft/sec	Γ ft^2/sec	$\bar{V}$	Re $= \dfrac{\Gamma}{\nu}$	a/R
Ring No. 1	.091	2.60	1.21	2.46	7780	.27
Ring No. 2	.111	13.5	6.07	3.10	37900	.075

The core diameter, 2a, is defined as the distance between the peak velocities on the $\dfrac{U}{U_o}$ versus r/r_o curve (Fig. 18).

REFERENCES

1. Yeh, Y., and Cummins, H., Appl. Phys. Lett. 4, pp. 176-8.

2. Goldstein, R. J. and Kreid, D. K., J. App. Mech. 34, pp 813.

3. Rudd, M. J., J. Phys E: Sci Instruments 2, Jan 1969, pp 55-8.

4. Lennert, A. E., Brayton, E. B. and Crosswy, F. L., "Summary Report of the Development of a Laser Velocimeter to be Used in AEDC Wind Tunnels," AEDC-TR-70-101, July 1970.

5. Iten, P. , Private Communication.

6. Widnall, S. E. and Sullivan, J. P. "On the Stability of Vortex Rings," submitted for publication.

7. Brodkey, P. S., The Phenomena of Fluid Motions, Addison-Wesley Publishing Company, 1967.
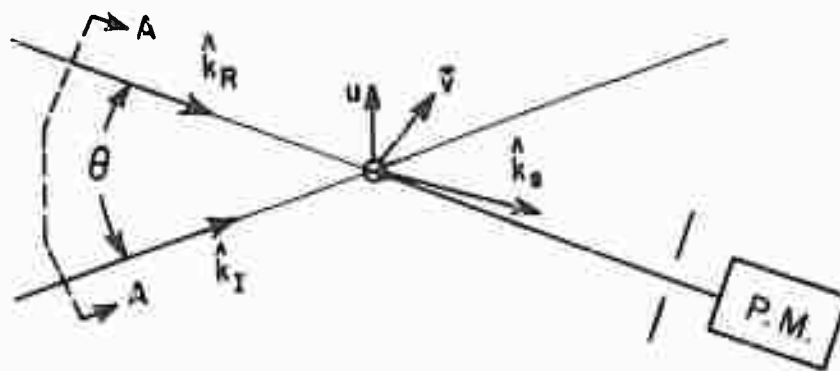
REFERENCE BEAM SYSTEM
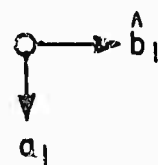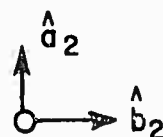
Fig. 1a

SECTION A-A
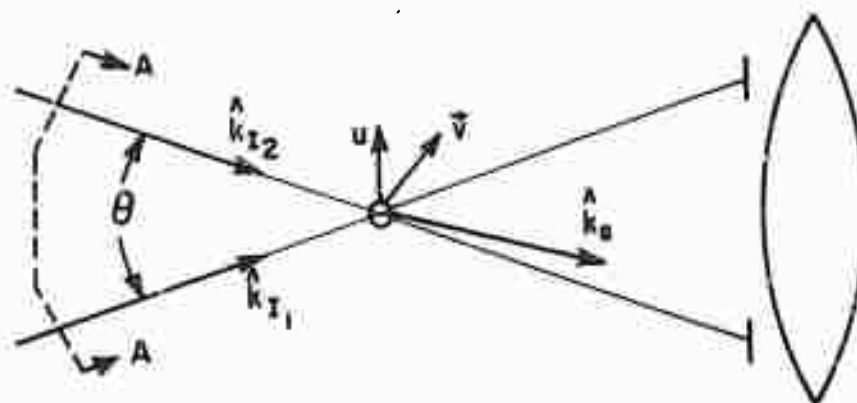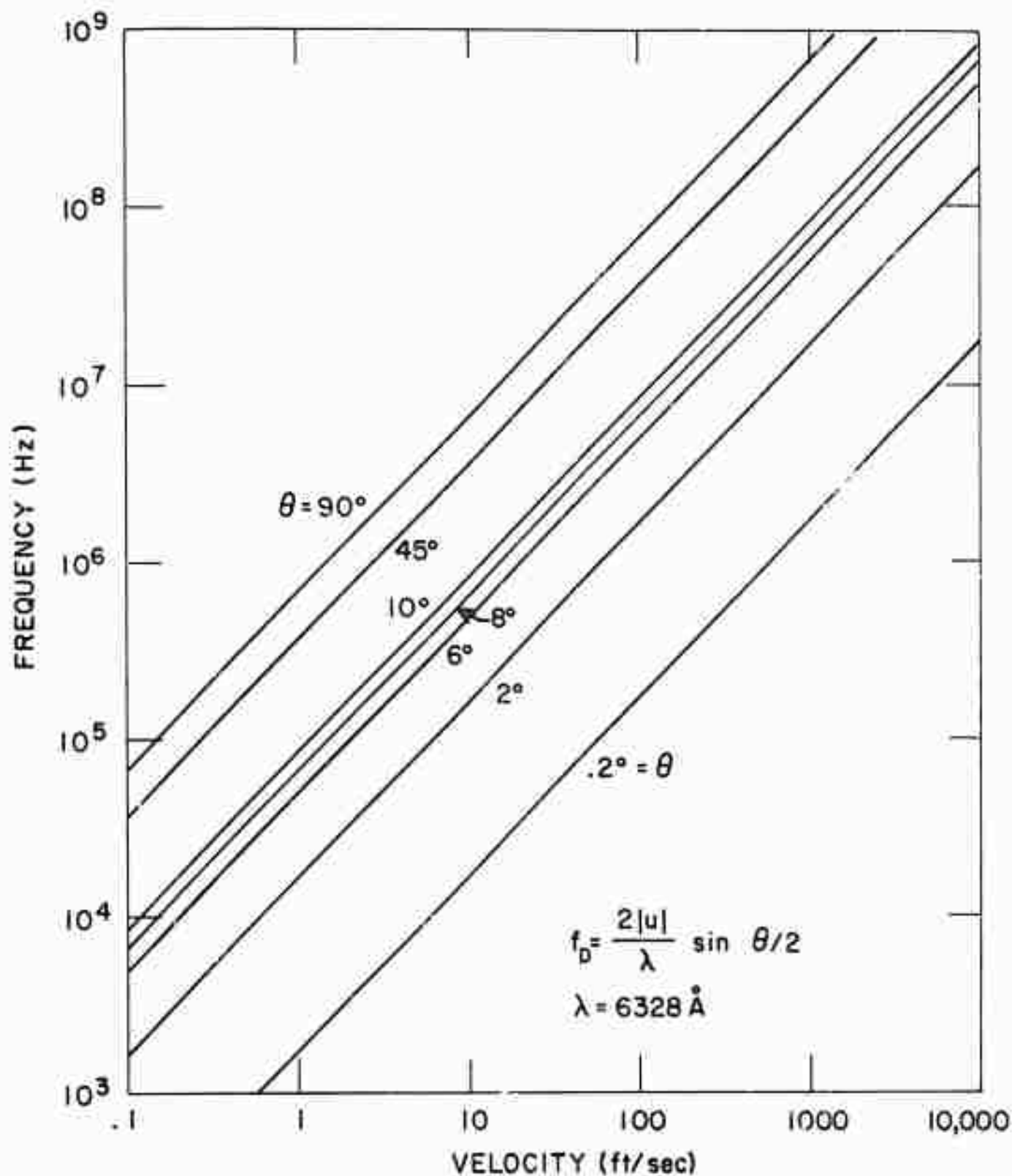
DUAL SCATTER SYSTEM

Fig. 1b

25

Fig. 2. Doppler shift vs. velocity for He-Ne laser at various scattering angles.

26
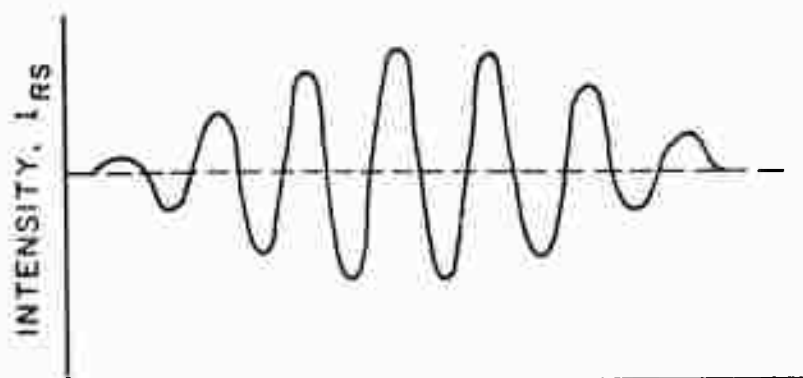
TIME

REFERENCE BEAM SYSTEM

Fig. 3a
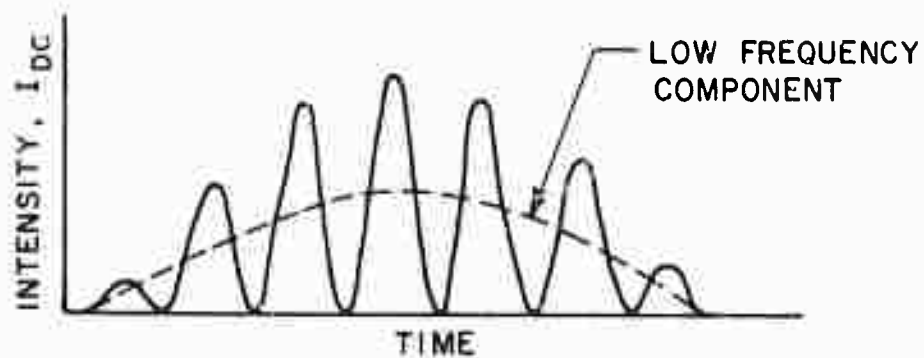
TIME

DUAL SCATTER SYSTEM

Fig. 3b

27
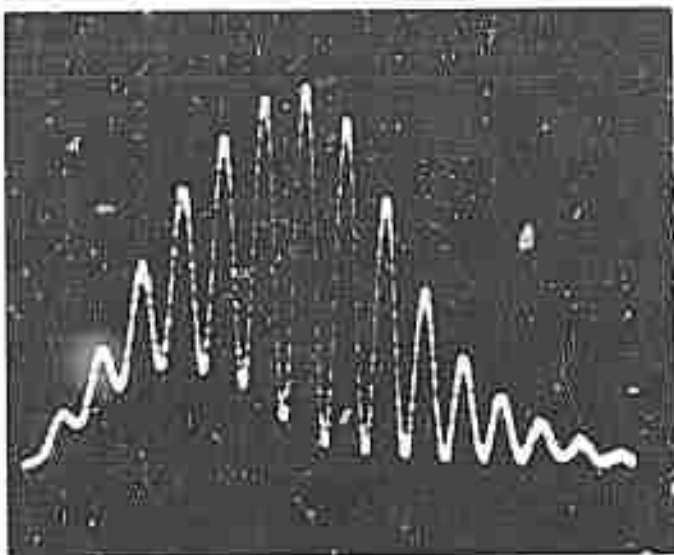
Fig. 4a. Doppler signal from .0002 dia. wire passing through center of probe volume. Vert.scale 100MV/cm Horiz. "   .1MS/cm
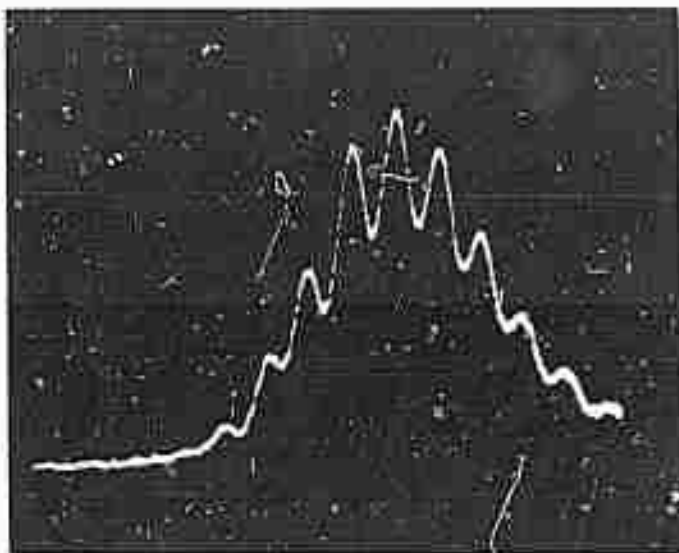
Fig. 4b. Doppler signal from .0002 dia. wire which did not pass through center of probe vol. Scale same as 4a.
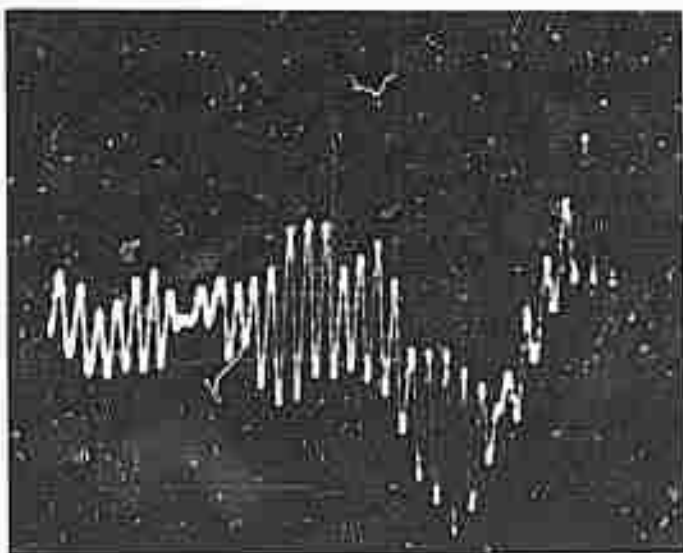
Fig. 4c. Doppler signal from spinning disk. Vert.scale 100MV/cm Horiz. "   50MS/cm

28

REFERENCE BEAM   DUAL SCATTER

0   500KHZ   0   500KHZ

1. Disk   1. Disk
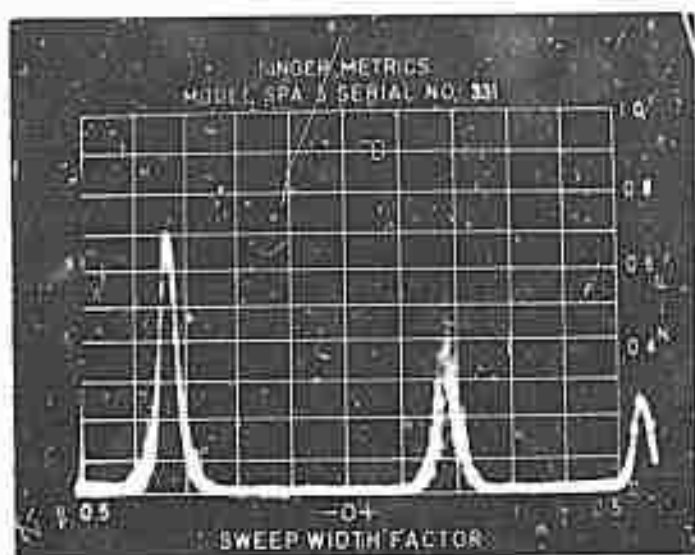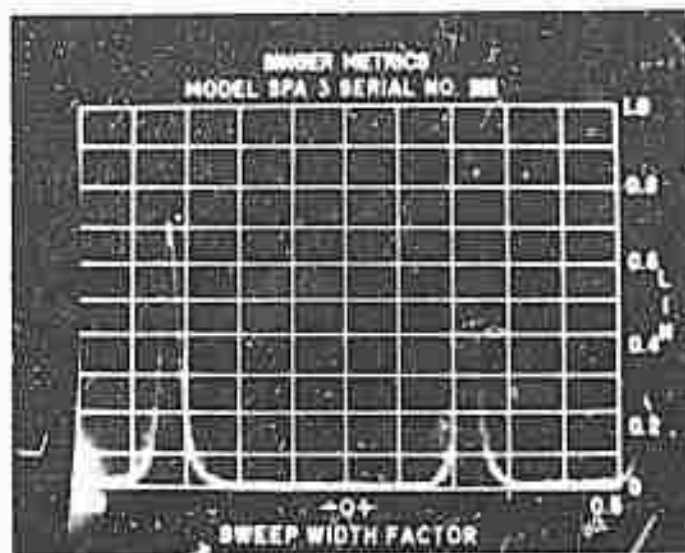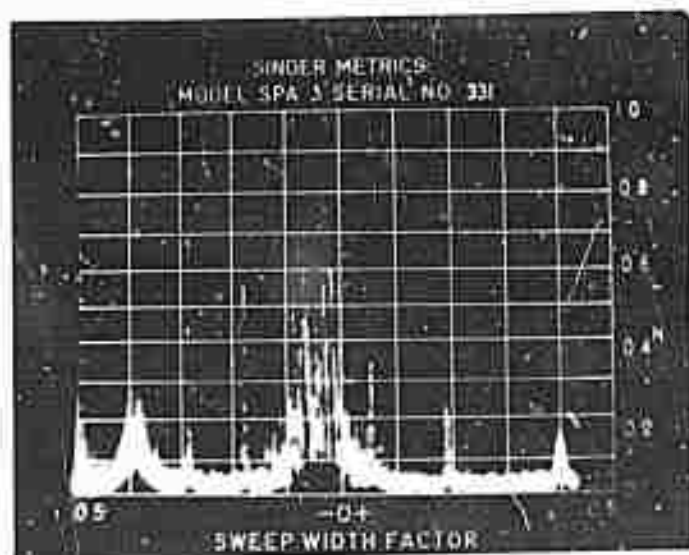
0   1MHZ   2MHZ   0   1MHZ   2 MHZ

    2. Smoke Jet   2. Smoke Jet

    Fig. 5. Signals from Ref. Beam & Dual Scatter Systems

29

Fig. 6. One Dimensional LDV System.

30
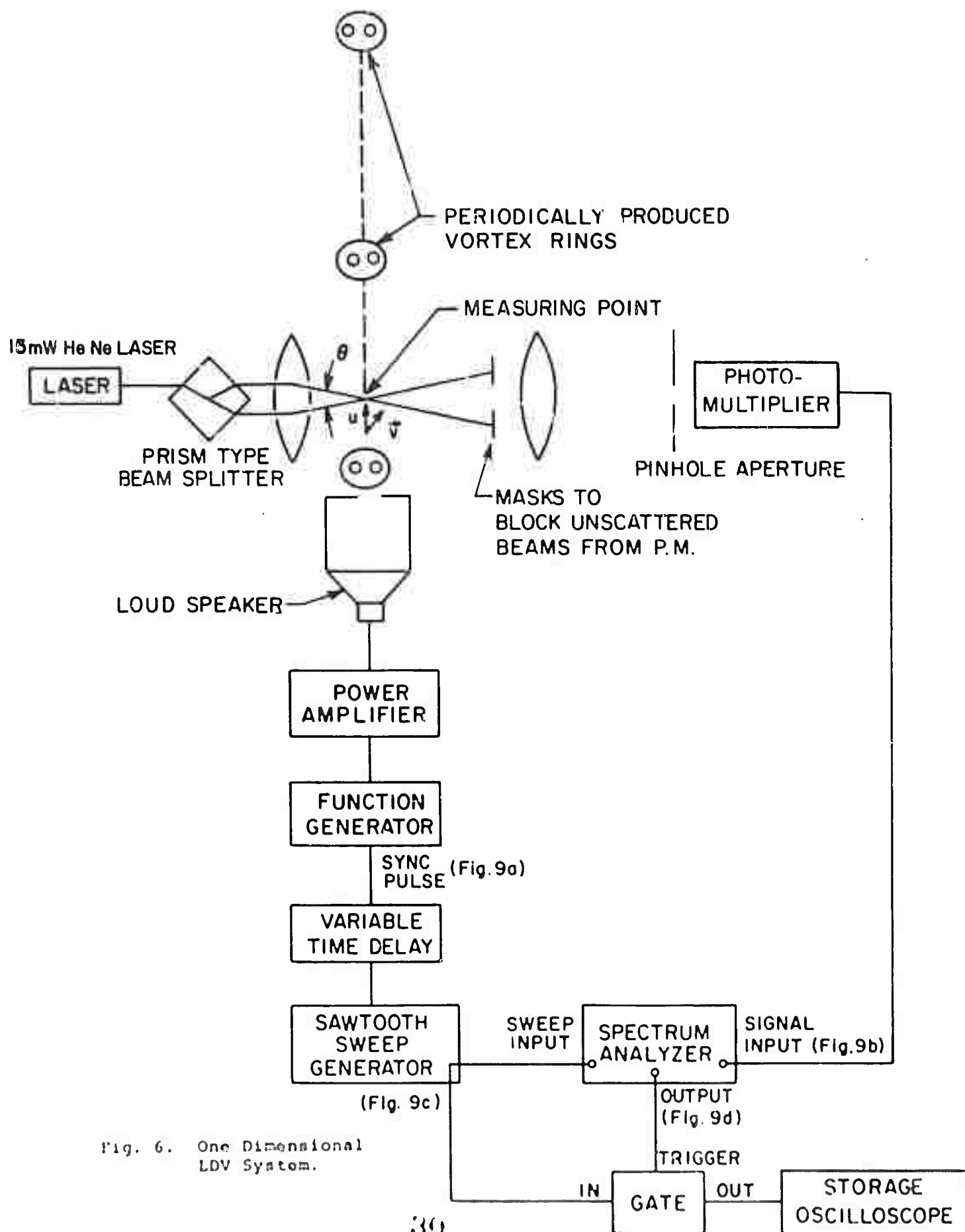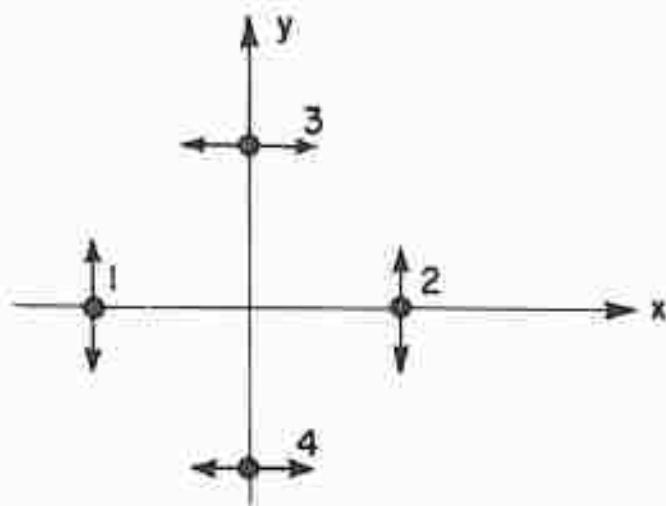
Fig. 7.   Beam pattern for two dimen-
          sional LDV looking toward
          laser.   The arrows indicate
          the direction of polariza-
          tion.   Beams 1 and 2 measure
          velocity component in the
          x direction and beams 3 and
          4 in the y direction.
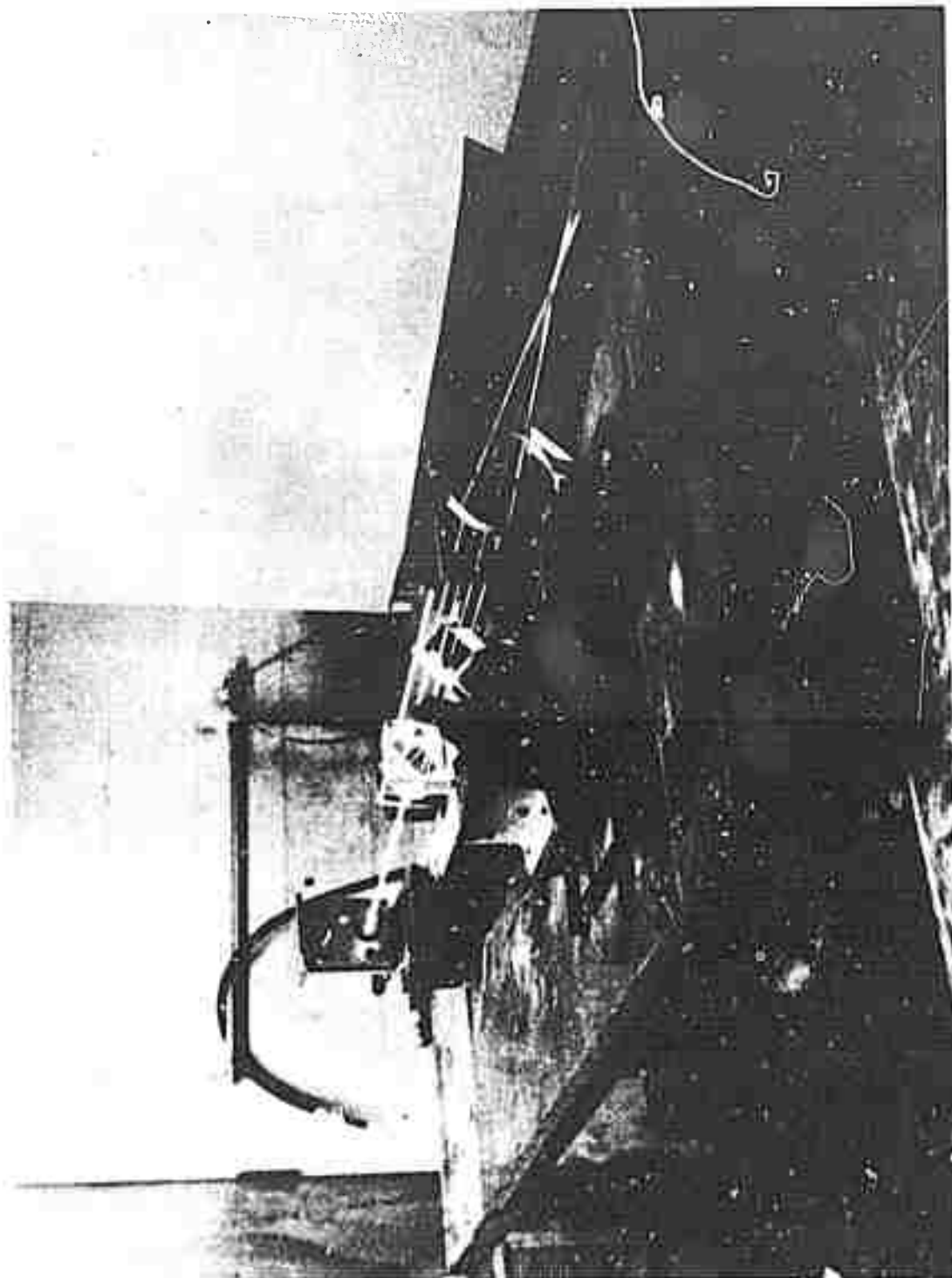
Fig. 8. Two-dimensional LDV system.
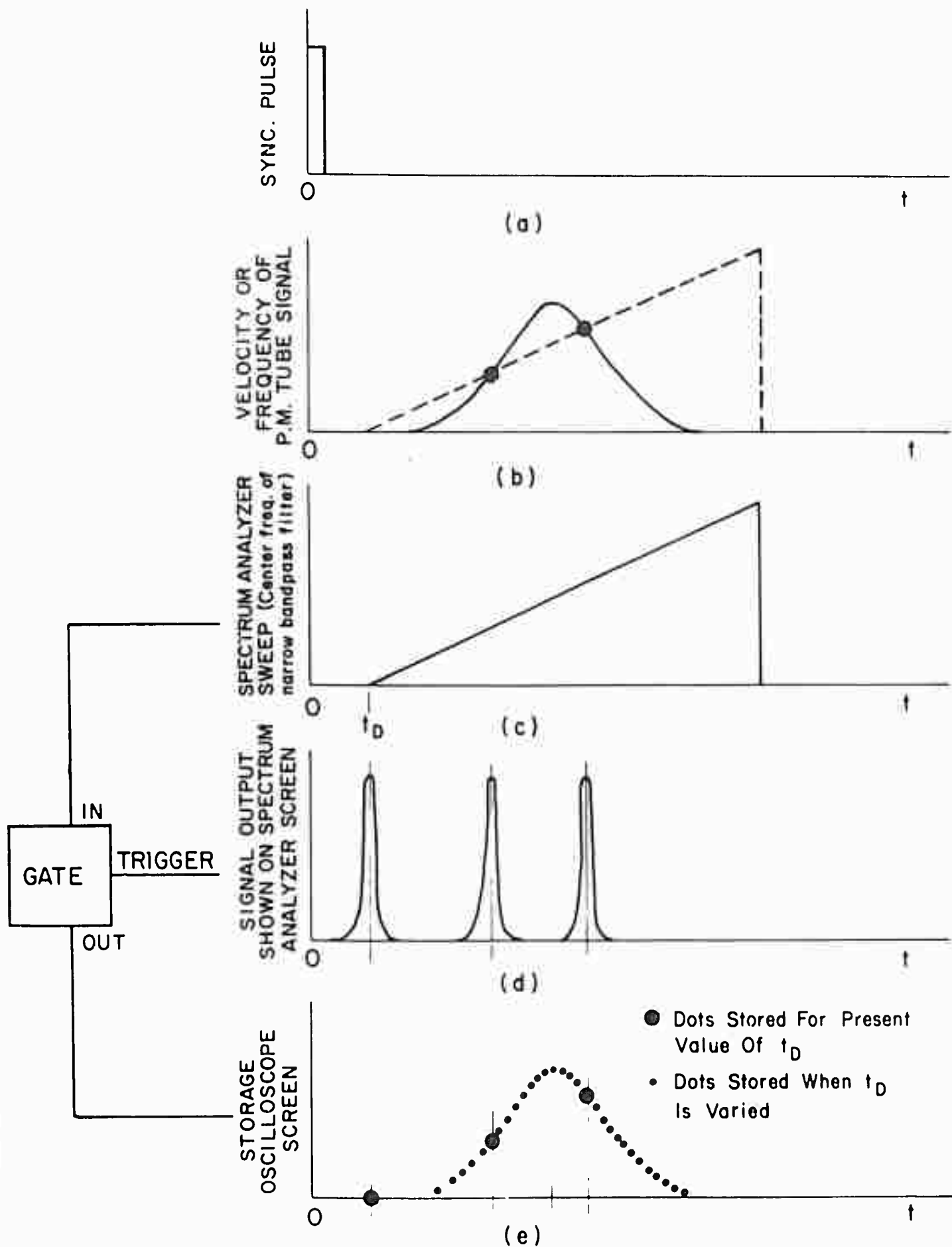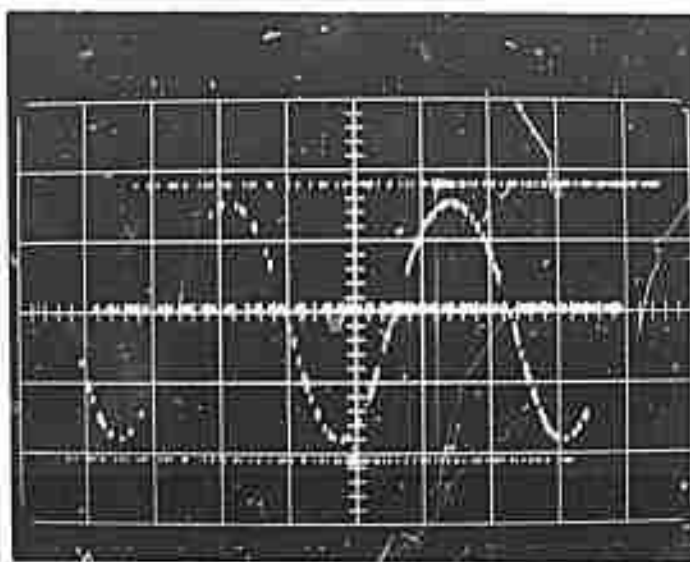
Fig. 9.   Time diagrams for electronic system.

33

Fig. 10.   Demodulation of Test Signal

$$f_O = 500 \text{ kHz}$$
$$Df = 450 \text{ kHz}$$
$$f_M = 33 \text{ cy/sec}$$

34
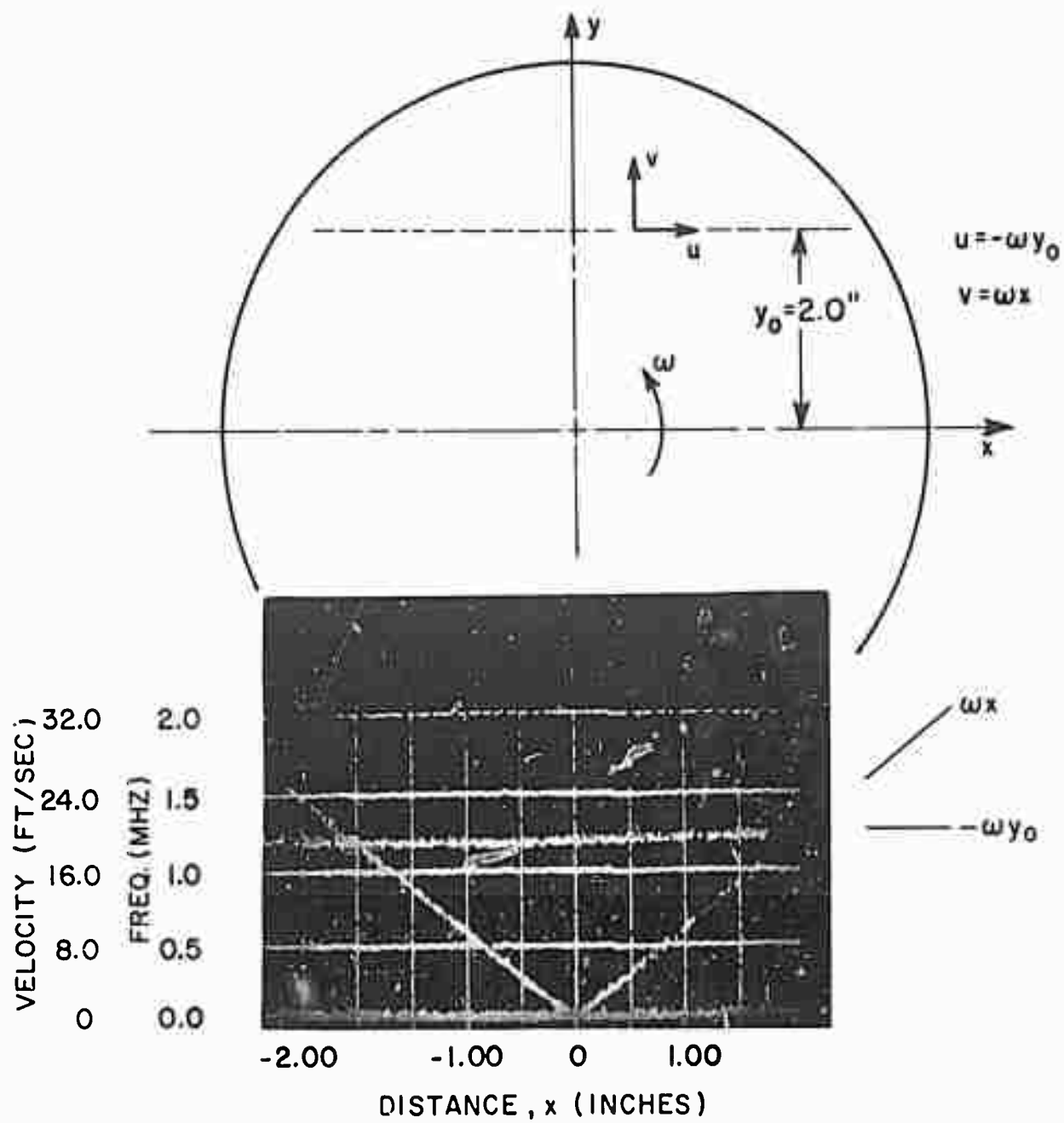
Fig. 11. Linearity and Velocity Check
Using Spinning Disk

35

Fig. 12. Vortex ring.

36
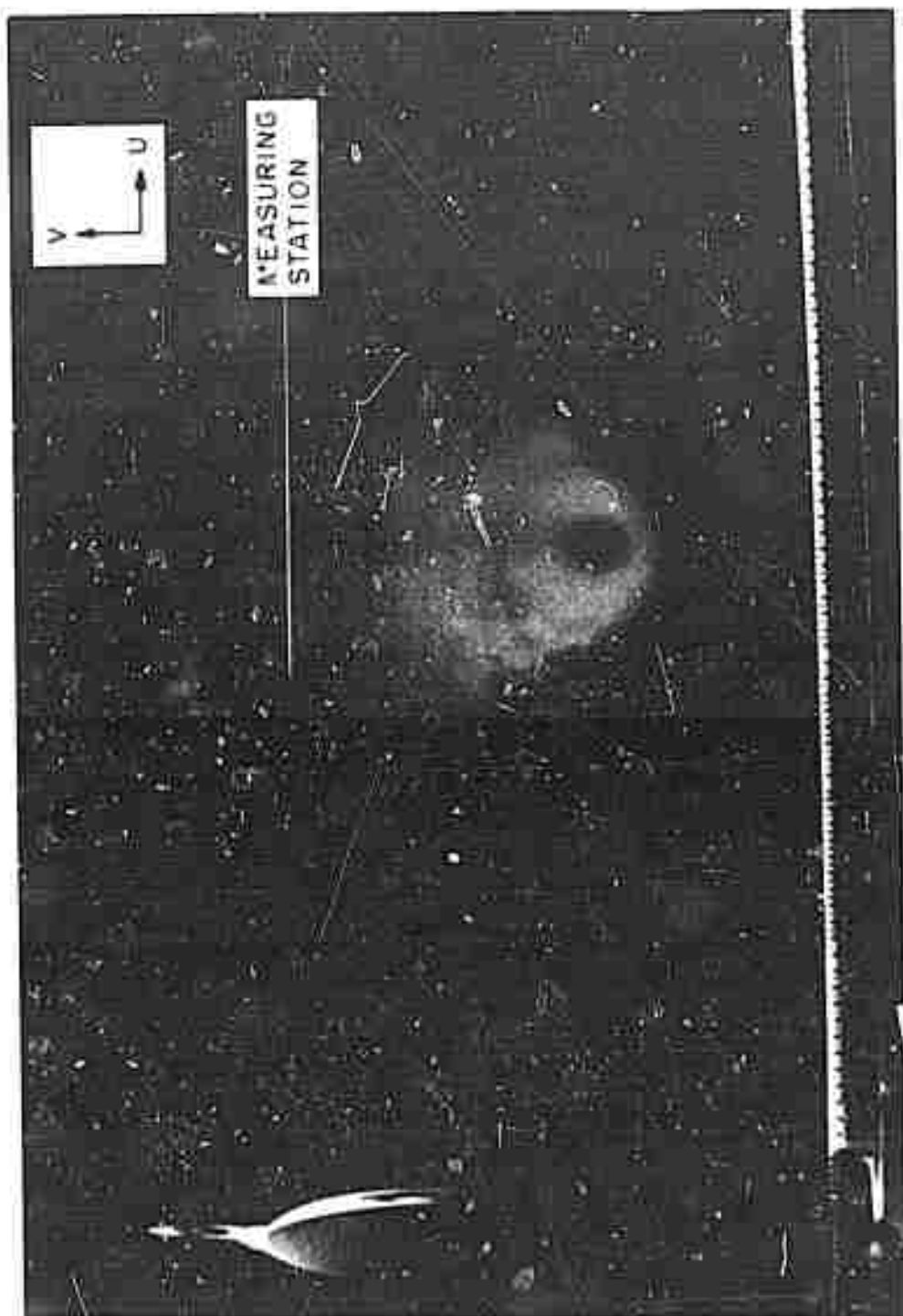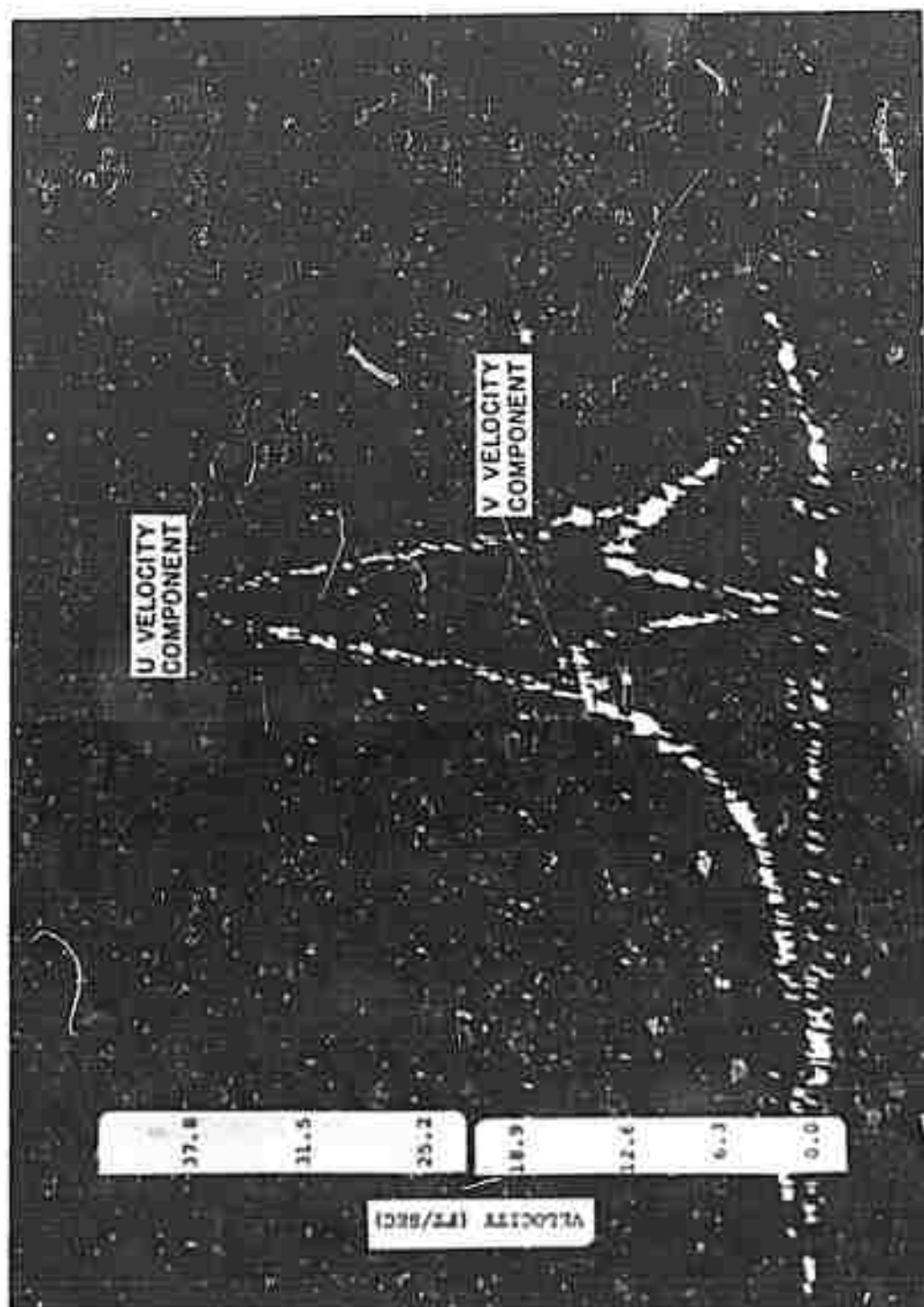
Fig. 13. Velocity distribution through vortex ring.
Time Scale: 5 ms/cm.

Note: All Data Presented—
Is on this Side of
Vortex Ring

Fig. 14.   Coordinate system for vortex ring data analysis.

38
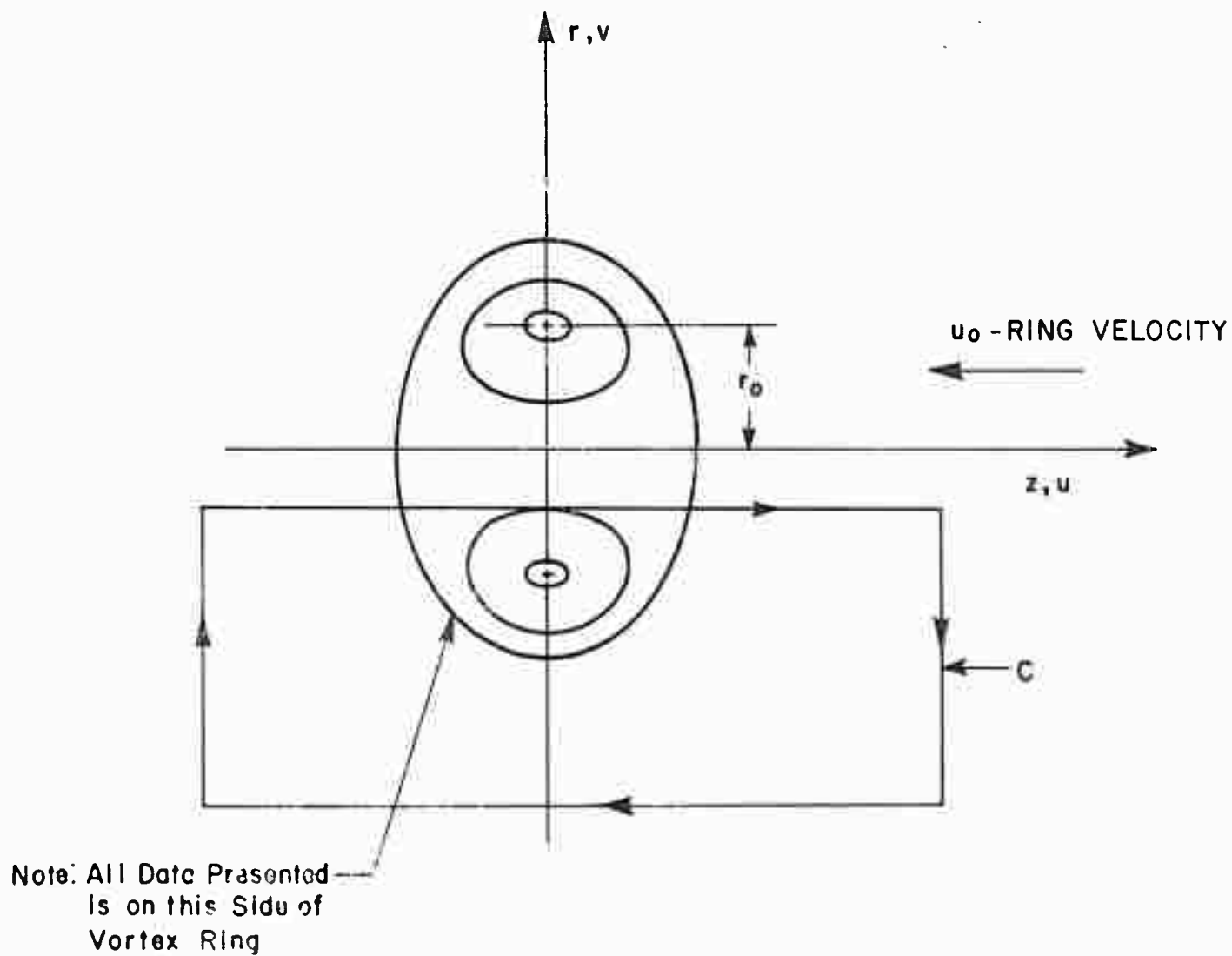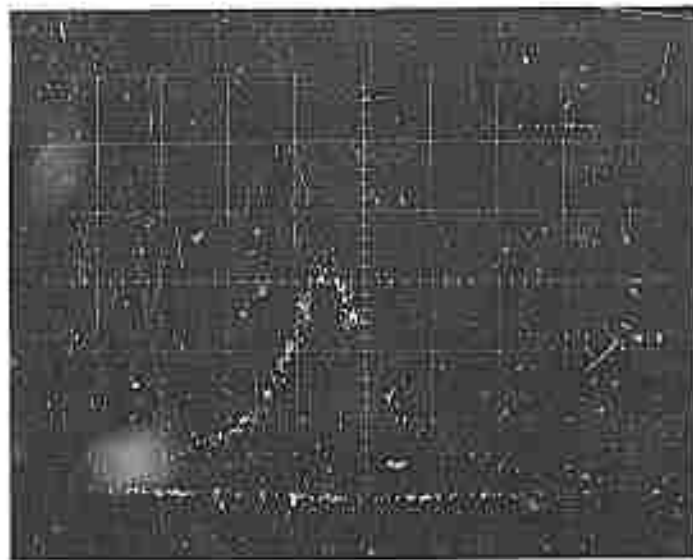
Fig. 15a. U component of velocity
at r/r_o = .876 for
Ring No. 1.
Time Scale 20 MS/cm
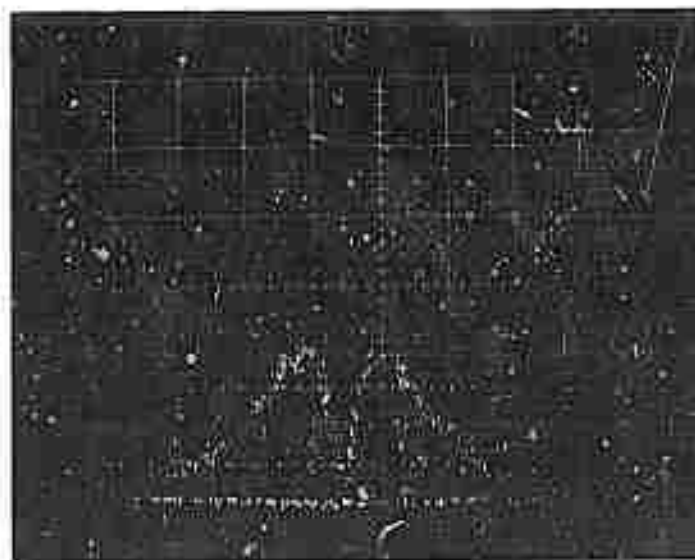
Fig. 15 b. V component of velocity
at r/r_o = -- 1.08 for
Ring No. 1.
Time Scale 20 MS/cm
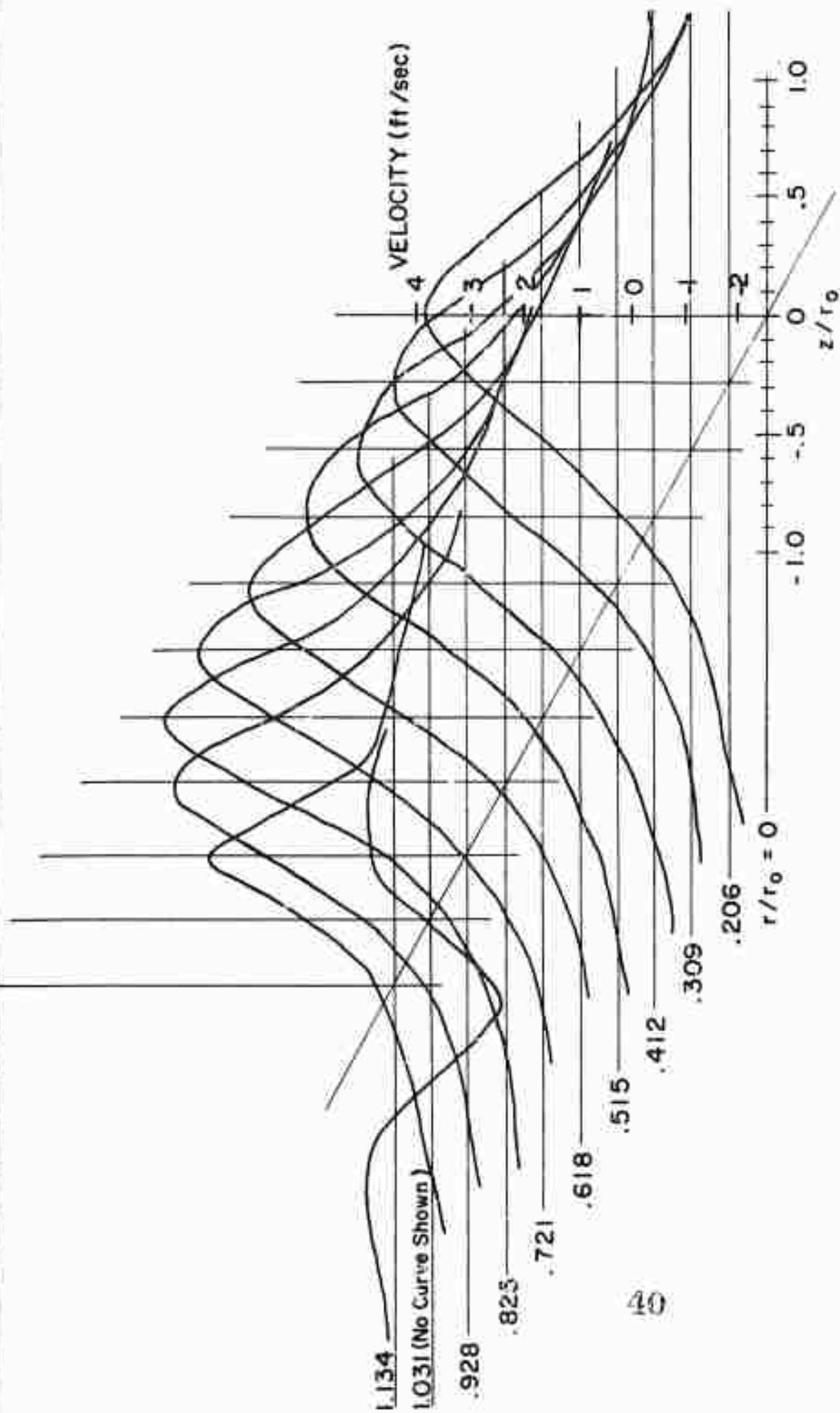
Fig. 16. U component of velocity versus axial distance at various radial stations of Ring No. 1.

40
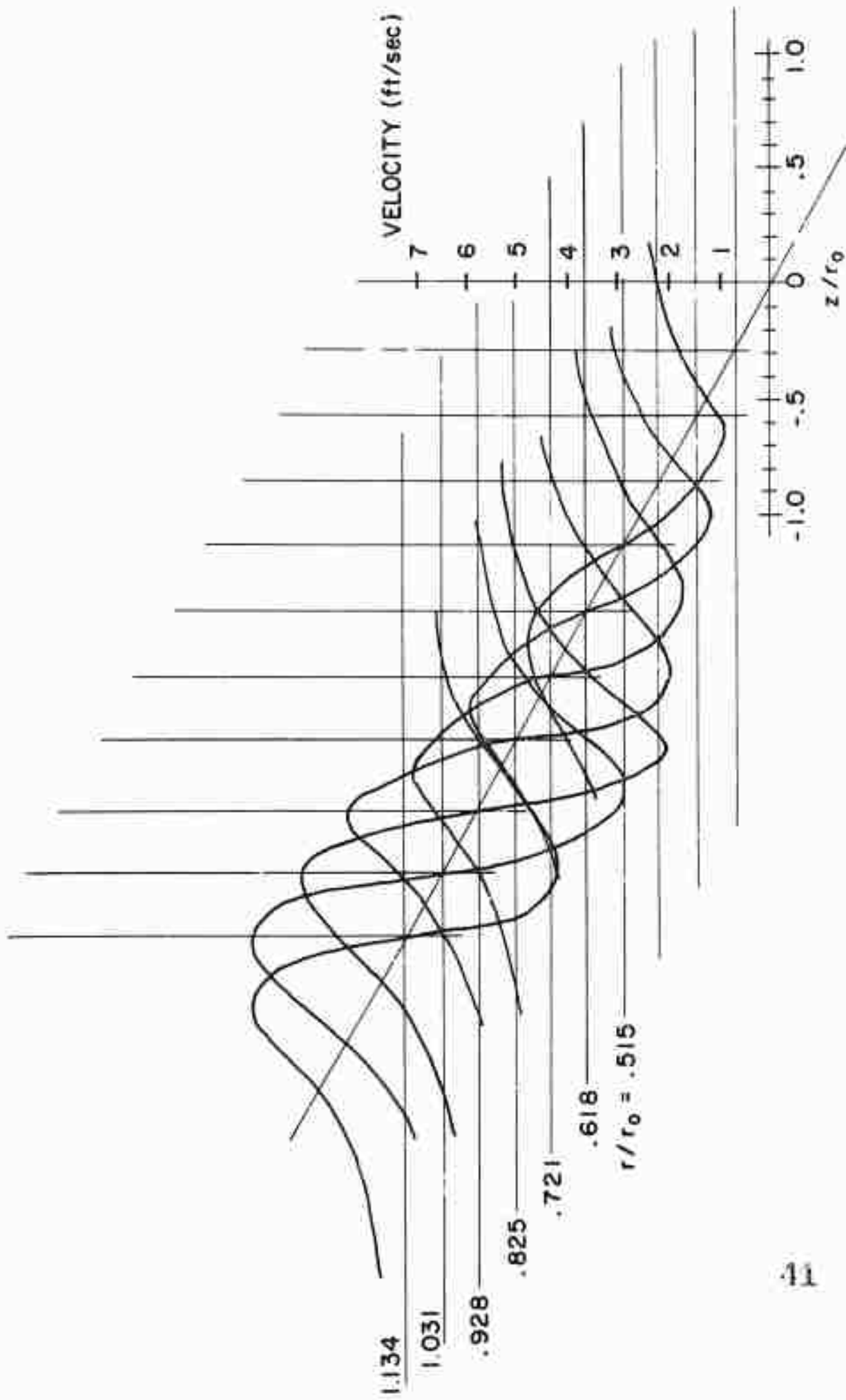
Fig. 17. V component versus axial distance at various radial stations of Ring No. 1.
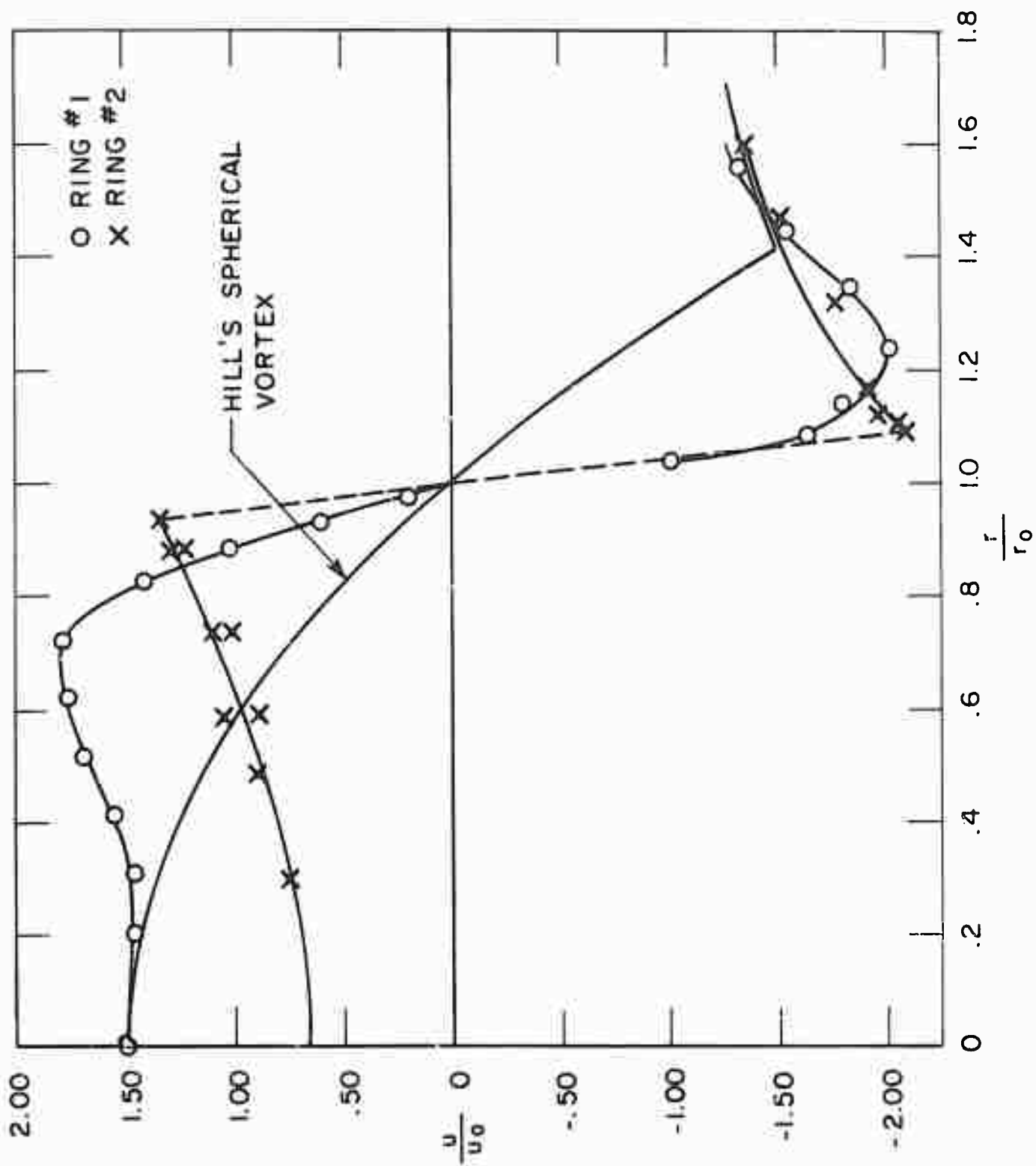
Fig. 18. U/u_o versus r/r_o along $z/r_o = 0$.
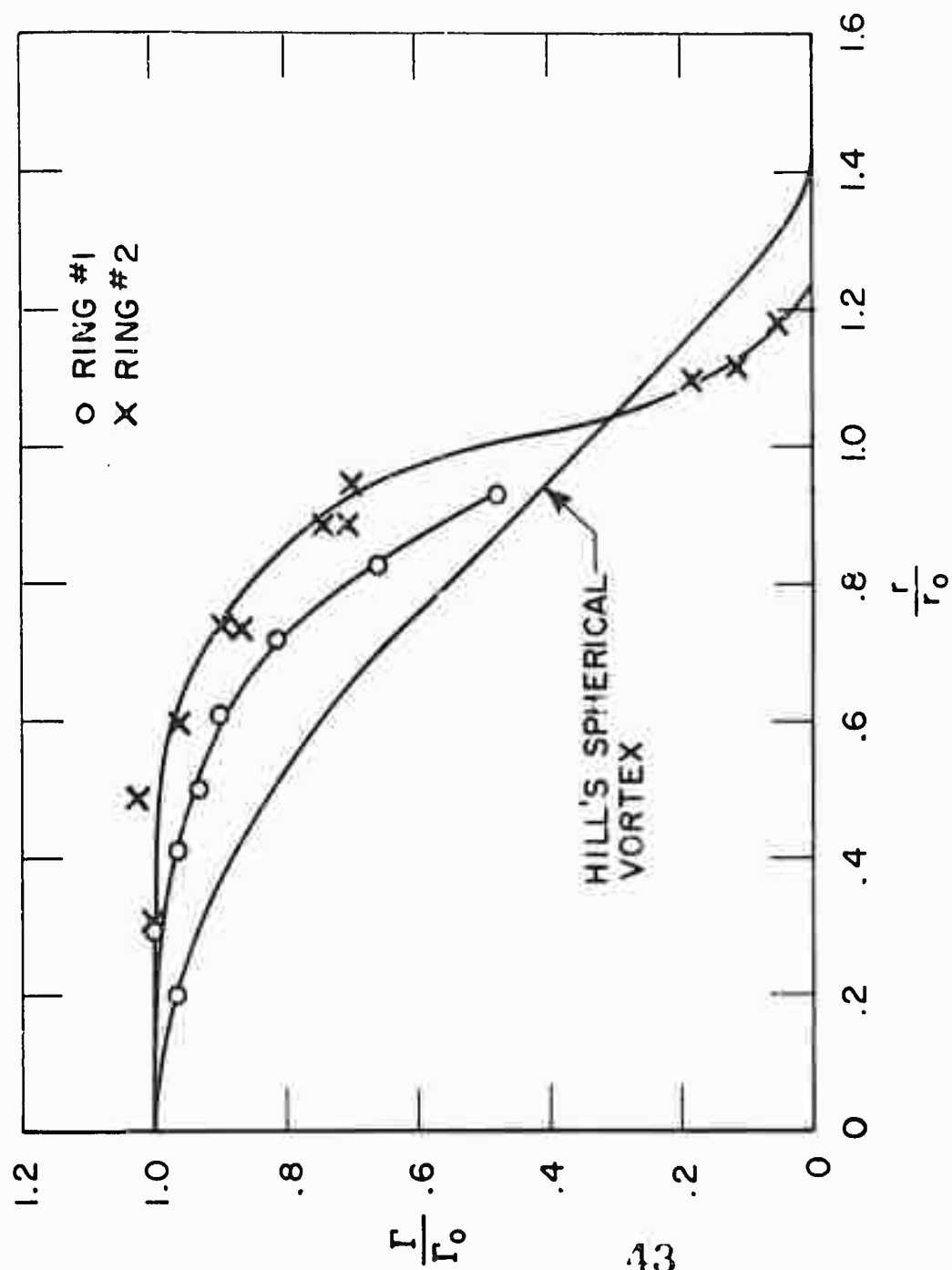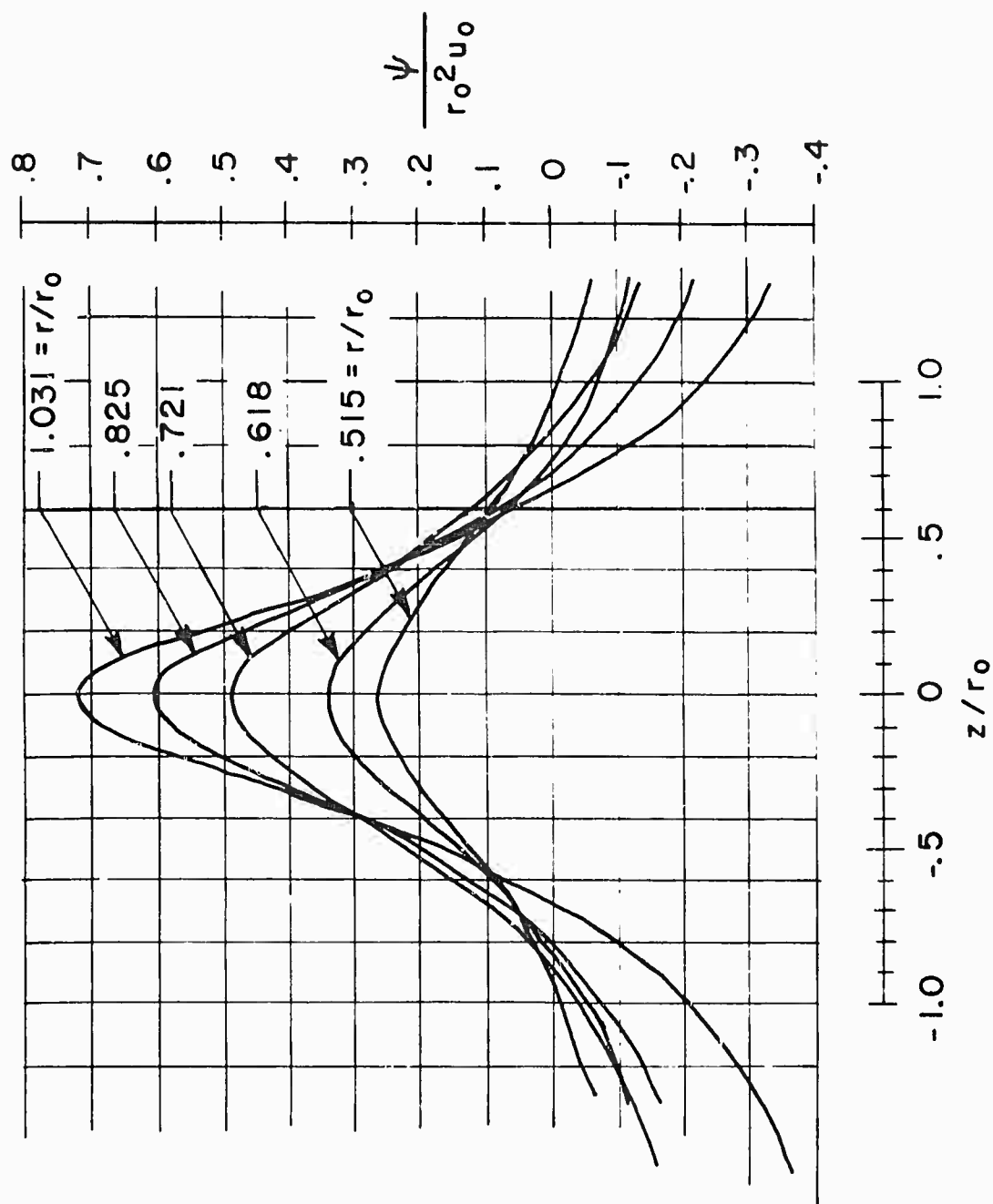
42

Fig. 19. Γ/Γ_o versus r/r_o.

43

Fig. 20. $\psi/r_o^2 u_o$ versus z/r_o at various radial stations

44

Fig. 21. $\psi/r_o^2 U_o$ versus r/r_o at $Z/r_o = 0$.
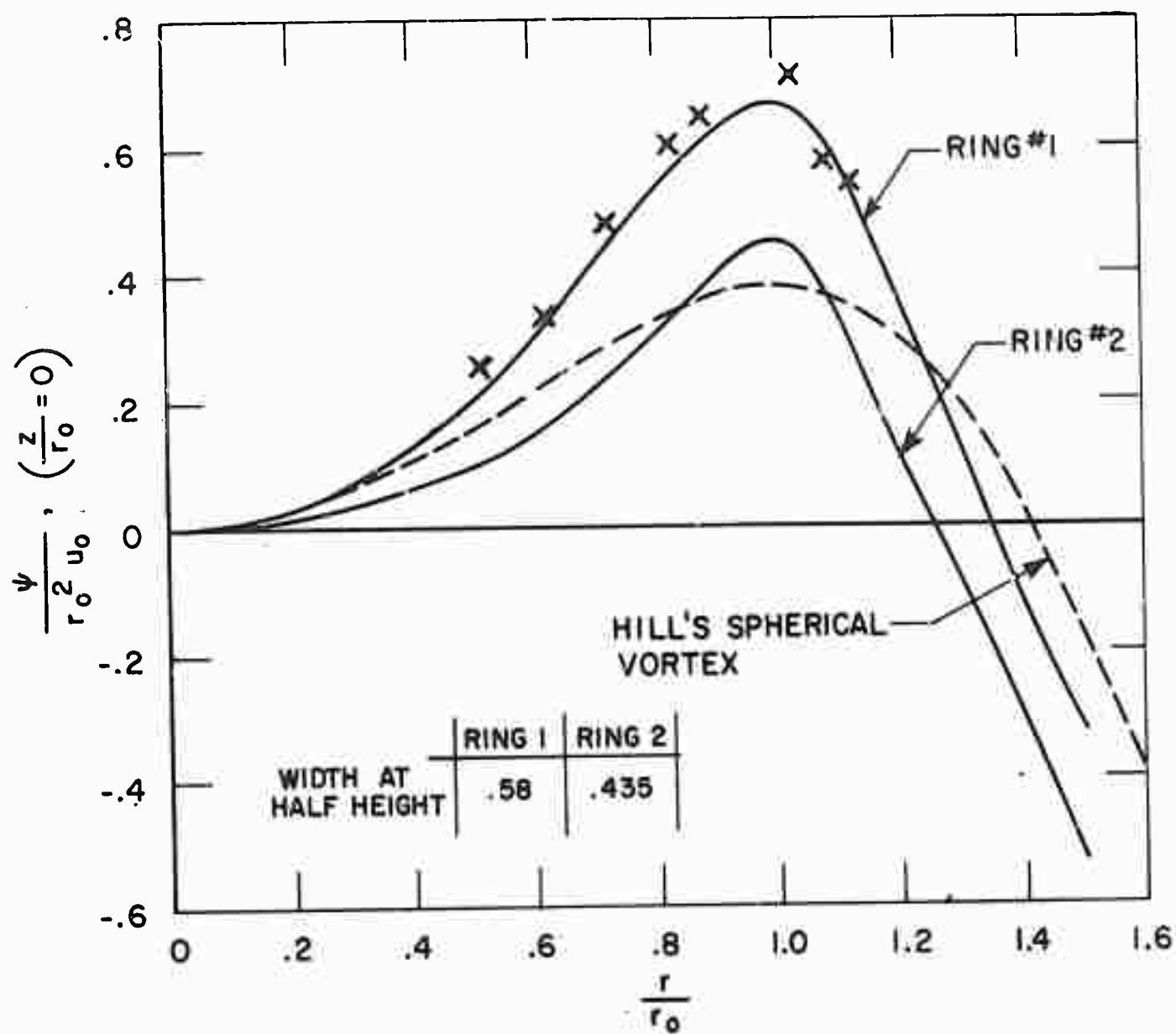
$\times$ - Calculated from Eq. 2.

Solid curves calculated from Eq. 3.

45
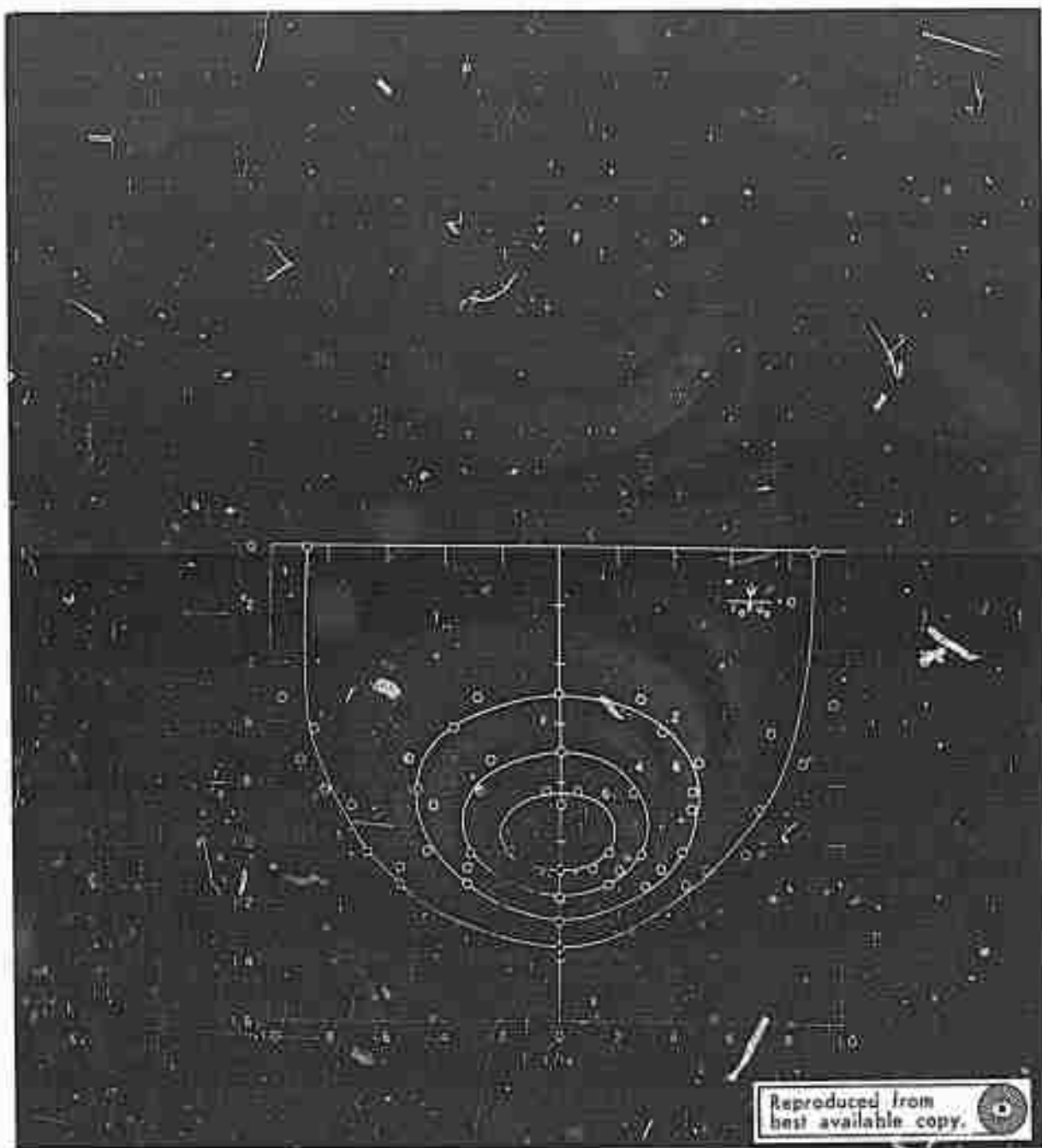
Fig. 22. Side view of ring No. 1 with measured
stream lines superposed.

46
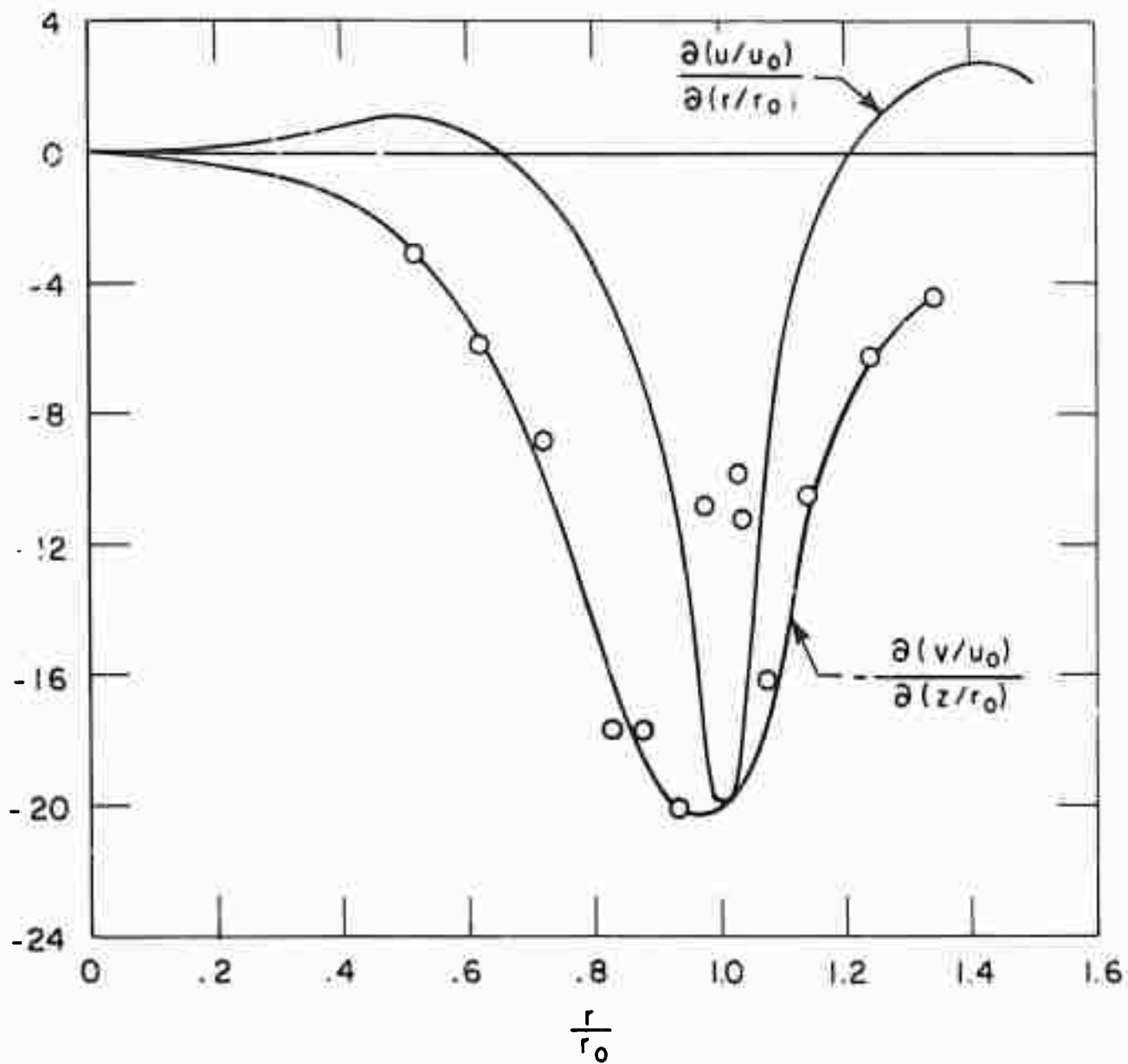
Fig. 23. Partial Derivatives Used For
Calculating the Vorticity.

47

Fig. 24. Vorticity $\dfrac{\omega}{U_o/r_o}$ versus r/r_o

48
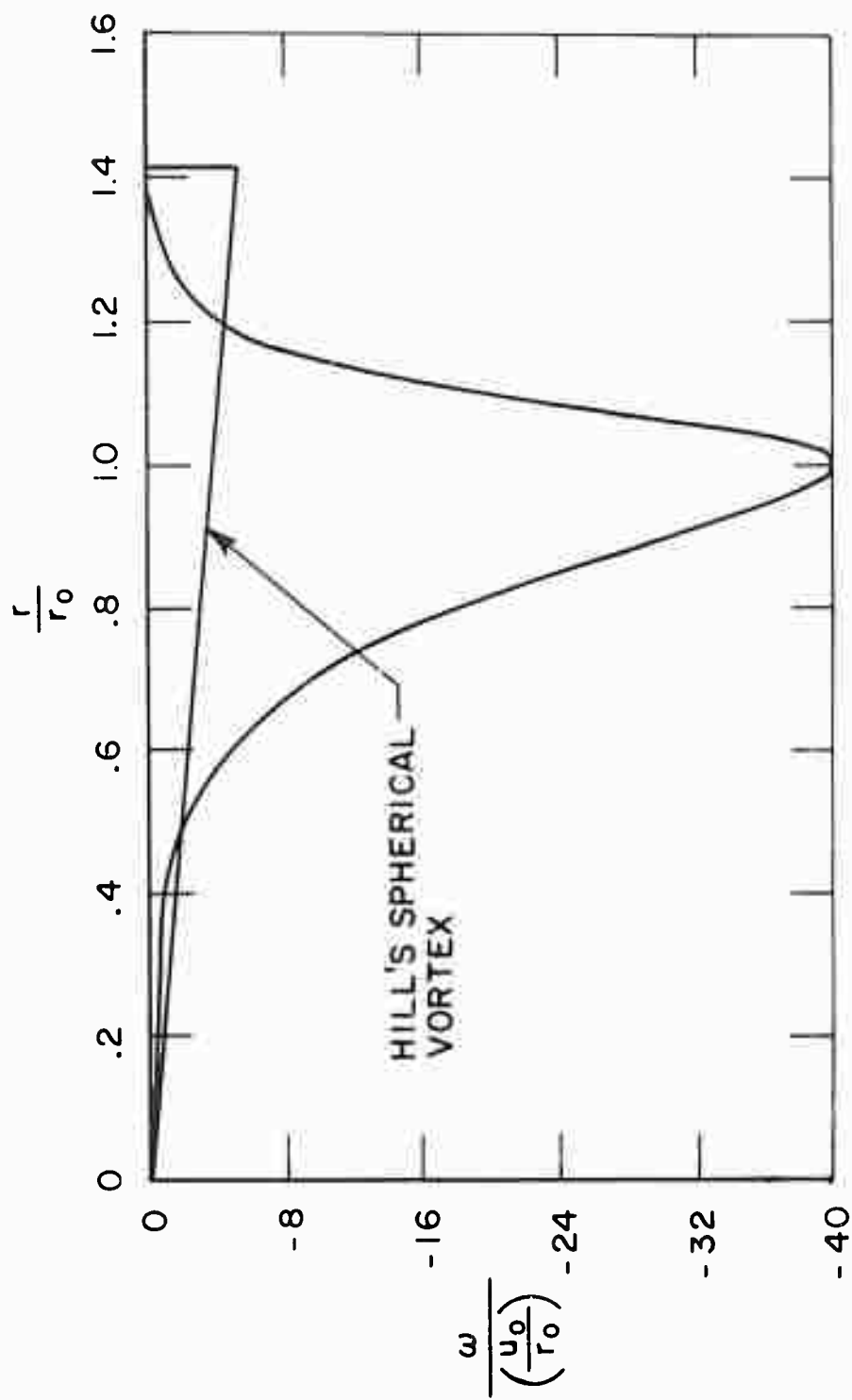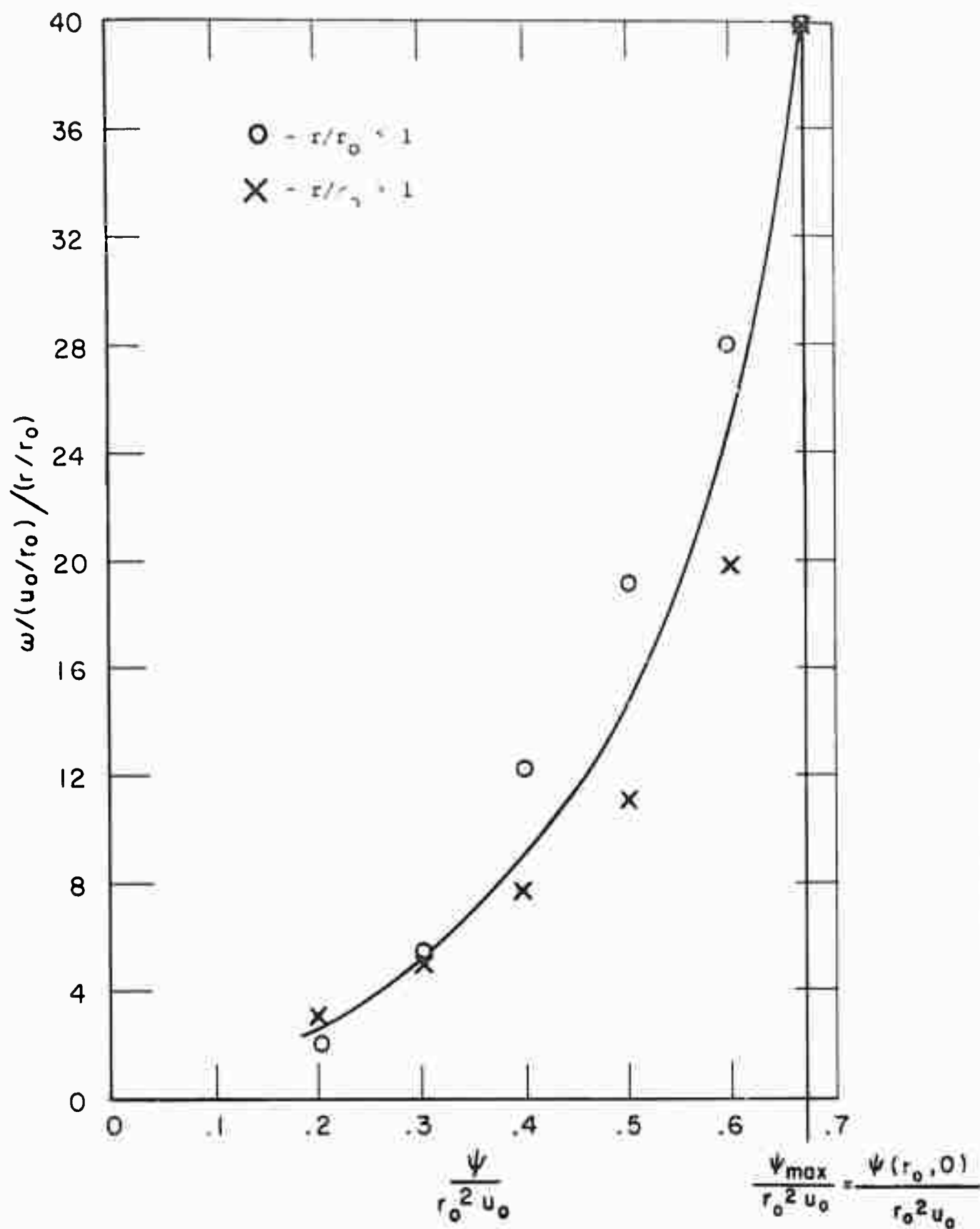
Fig. 25. Non-dimensional ω/r versus ψ.

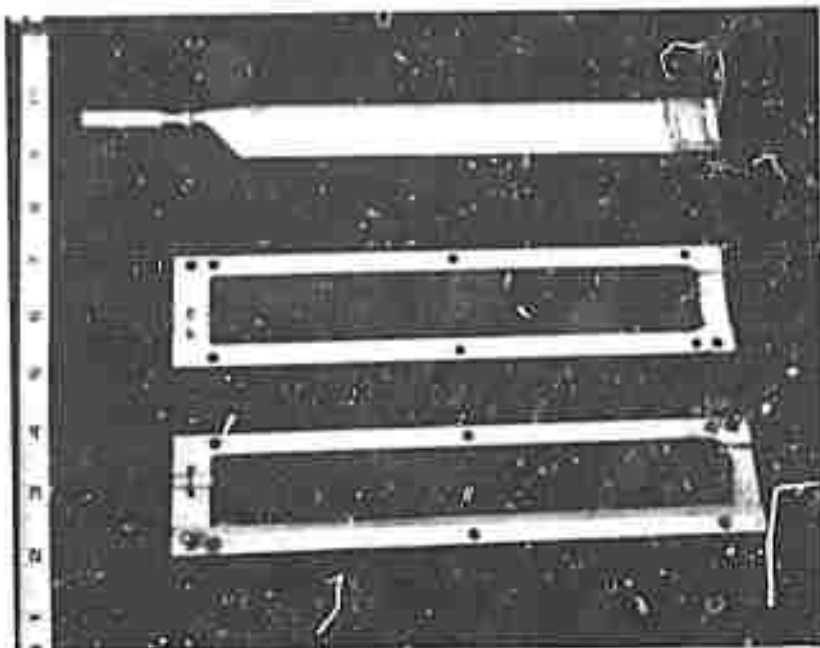49
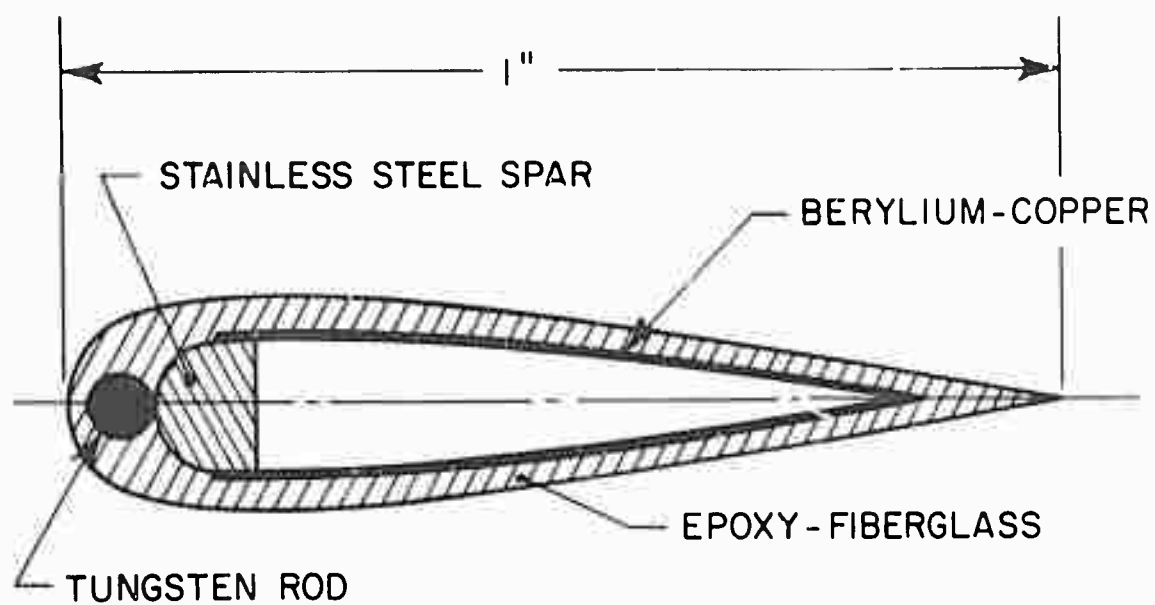
Fig. 26. Cross Section of Blade - NACA 0012.

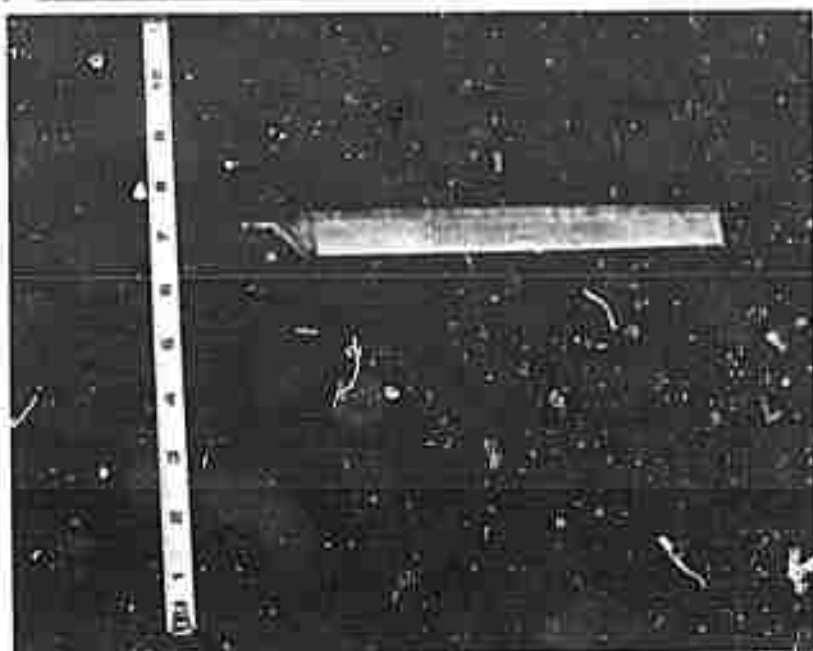Fig. 27a. Aluminum model and epoxy mold.

Fig. 27b. Finished blade.
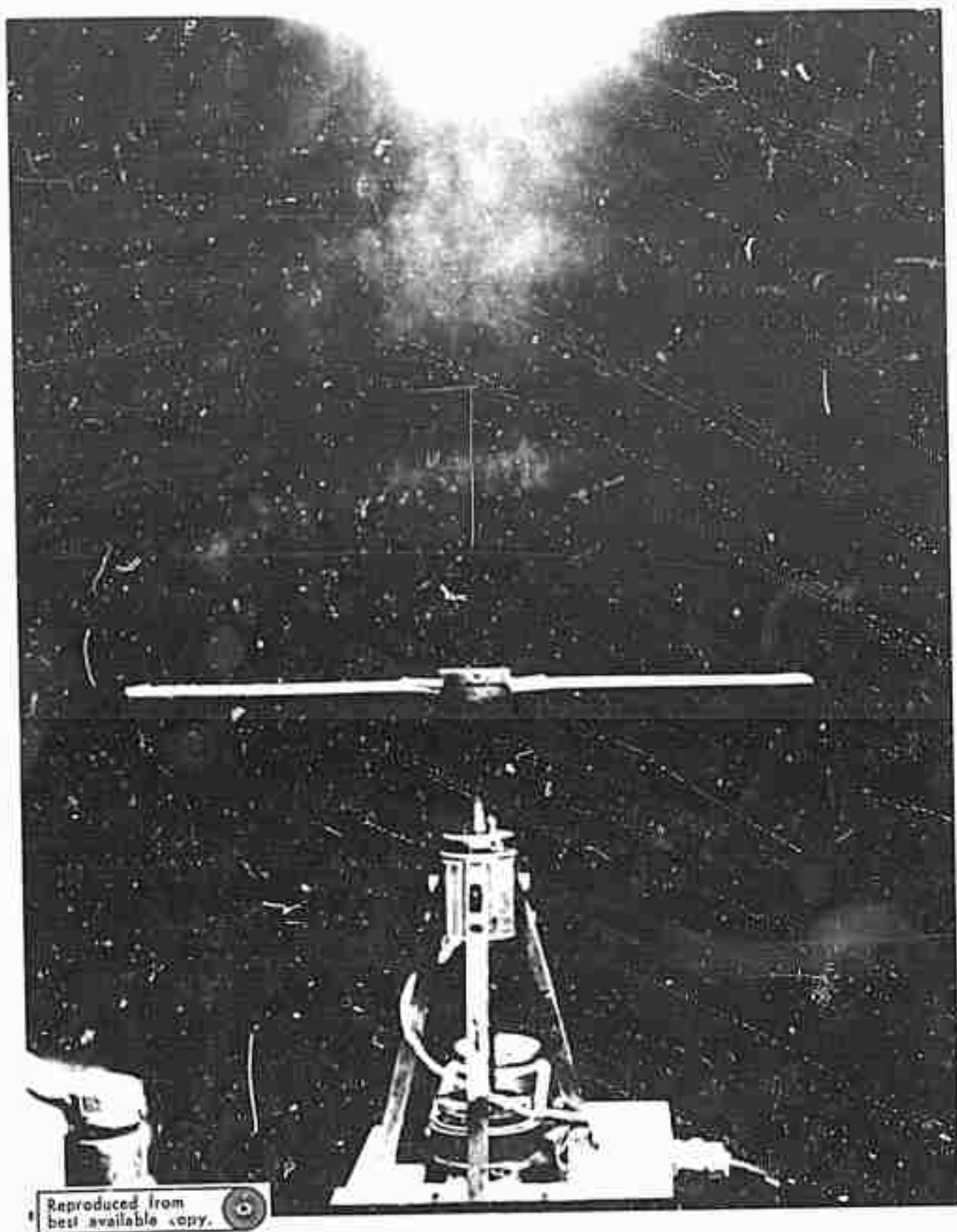
Fig. 27c. End view of finished blade.

51

Fig. 28.   Hovering rotor at 3200 rpm with smoke
ejected at rotor tips.

52